

# Multiscale Modeling of Hematologic Disorders

Dmitry Fedosov, Igor Pivkin, Wenxiao Pan, Ming Dao, Bruce Caswell, and  
George Em Karniadakis

**Abstract** Parasitic infectious diseases and other hereditary hematologic disorders are often associated with major changes in the shape and viscoelastic properties of red blood cells (RBCs). Such changes can disrupt blood flow and even brain perfusion, as in the case of cerebral malaria. Modeling of these hematologic disorders requires a seamless multiscale approach, where blood cells and blood flow in the entire arterial tree are represented accurately using physiologically consistent parameters. In this chapter, we present a computational methodology based on dissipative particle dynamics (DPD) which models RBCs as well as whole blood in health and disease. DPD is a Lagrangian method that can be derived from systematic coarse-graining of molecular dynamics but can scale efficiently *up* to small arteries and can also be used to model RBCs *down* to spectrin level. To this end, we present two complementary mathematical models for RBCs and describe a systematic procedure on extracting the relevant input parameters from optical tweezers and microfluidic experiments for single RBCs. We then use these validated RBC models to predict the behavior of whole healthy blood and compare with experimental

---

Dmitry Fedosov

Forschungszentrum Jülich, 52425 Jülich, Germany e-mail: d.fedosov@fz-juelich.de

Igor Pivkin

Massachusetts Institute of Technology, Cambridge, MA 02139 e-mail: piv@mit.edu, currently at University of Lugano, Via Giuseppe Buffi 13, CH-6904, Lugano, Switzerland, e-mail: igor.pivkin@usi.ch

Wenxiao Pan

Pacific Northwest National Laboratory, Richland, WA 99352 e-mail: Wenxiao.Pan@pnl.gov

Ming Dao

Massachusetts Institute of Technology, Cambridge, MA 02139 e-mail: mingdao@mit.edu

Bruce Caswell

Brown University, Providence, RI 02912 e-mail: caswell@dam.brown.edu

George Em Karniadakis

Brown University, Providence, RI 02912 e-mail: George\_Karniadakis@brown.edu

results. The same procedure is applied to modeling malaria, and results for infected single RBCs and whole blood are presented.

## 1 Introduction

The healthy human red blood cells (RBCs) are discocytes when not subjected to any external stresses and they are approximately 7.5 to 8.7  $\mu\text{m}$  in diameter and 1.7 to 2.2  $\mu\text{m}$  in thickness (31). The membrane of the RBC is made up of a phospholipid bilayer and a network of spectrin molecules (cytoskeleton), with the latter largely responsible for the shear elastic properties of the RBC. The spectrin network is connected to bilayer via transmembrane proteins and together with the spectrin filaments and the cytosol inside the membrane determine the morphological structure of RBCs. This critical binding between the spectrin network and the lipid bilayer is actively controlled by ATP (64). Parasitic infections or genetic factors can drastically change the viscoelastic properties and even the shape of RBCs (10). For example, the parasite *Plasmodium falciparum* that invades the RBCs (Pf-RBCs) of most malaria patients affects drastically the RBC membrane properties resulting in a ten-fold increase of its shear modulus and a spherical shape at the later stages of the intra-cell parasite development (10). In addition, Pf-RBCs develop knobs on their surface that serve as adhesion sites for the binding to other Pf-RBCs as well as healthy RBCs. This enhanced cytoadherence of Pf-RBCs in combination with their reduced deformability may cause blood flow obstruction especially through the smaller arterioles and capillaries. Sick cell anemia is another blood disorder that affects the hemoglobin inside the RBCs causing dramatic changes in their shape and deformability. These changes combined with the increased internal viscosity affects the flow of sickled RBCs through the capillaries leading to flow occlusion (10, 38). Other hereditary diseases with similar effects are spherocytosis and elliptocytosis (3). In the former, RBCs become spherical with reduced diameter and carry much more hemoglobin than healthy RBCs. In the latter, RBCs are elliptical or oval in shape and of reduced deformability.

The common problem in the aforementioned hematologic disorders is the remodeling of the cytoskeleton and correspondingly a change in the structure and viscoelastic properties of individual RBCs, so studying their mechanical and rheological properties in vitro can aid greatly in the understanding and possible discovery of new treatments for such diseases. To this end, new advanced experimental tools are very valuable in obtaining the basic properties of single RBCs in health and disease, which are required in formulating multiscale methods for modeling blood flow in vitro and in vivo. Specifically, advances in experimental techniques now allow measurements down to the nanometer scale, and include micropipette aspiration (12, 87), RBC deformation by optical tweezers (6, 37, 82), optical magnetic twisting cytometry (54), three-dimensional measurement of membrane thermal fluctuations (65, 69), and observations of RBCs immersed in both shear and in pressure-driven flows (1, 29, 75, 83, 85). Micropipette aspiration and optical tweezers techniques

tend to deform the whole RBC membrane directly, while optical magnetic twisting cytometry and measurements of membrane thermal fluctuations probe the membrane properties locally. The macroscopic shear modulus of healthy cells is reported in the range of  $2 - 12 \mu\text{N}/\text{m}$  from the two former techniques, while the two latter ones allow measurements of local rheological properties (e.g., the complex modulus).

These experiments provide sufficient evidence for a complex membrane mechanical response including its unique viscoelastic properties. In addition, Li et al. (47) suggest that metabolic activity or large strains may induce a continuous rearrangement of the erythrocyte cytoskeleton. Consequently, in their numerical model the RBC membrane may exhibit strain hardening or softening depending on certain conditions. Moreover, the cytoskeleton attachments can diffuse within the lipid bilayer, but such behavior can be neglected at short time scales. Gov (32) proposed an active elastic network model, where the metabolic activity may affect the stiffness of the cell through the consumption of ATP. The activity induced by ATP would also greatly affect membrane undulations (33, 64) resulting in fluctuations comparable to an effective temperature increase by a factor of three. For parasitic infectious diseases, powerful imaging techniques have been developed in recent years, which allow to observe details of parasite development inside the RBC and also to gain information about the properties of the cell components (50, 65). Figure 1(a) shows the parasite *P. falciparum* inside an infected RBC during the ring stage of parasite development, which was obtained using soft x-ray imaging technique. The parasite and some elaborate structure, which extends from the parasite into the cell cytosol, can be clearly seen in the image.

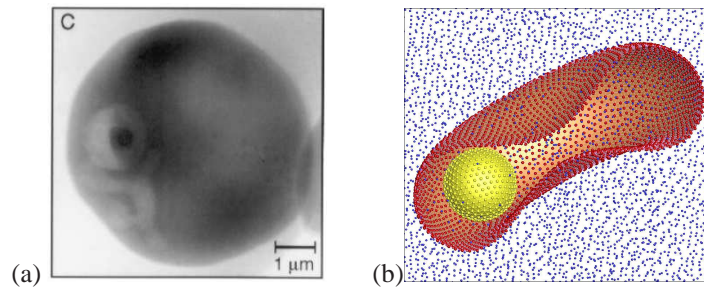


**Fig. 1** (a) Soft x-ray micrograph of intra-erythrocytic ring stage *P. falciparum* malaria parasite imaged in RBC (Reproduced from (50)). (b) The computational RBC model consists of particles connected with links. The model is immersed into DPD fluid and fully interacts with it through pairwise forces. The internal DPD fluid has a higher viscosity to match the viscosity of RBC cytosol. The *P. falciparum* parasite is modeled as a rigid sphere of two microns in diameter.

A number of numerical models have been developed recently including a continuum description (15, 20, 31, 70) and a discrete approximation on the spectrin molecular level (11, 46) as well as on the mesoscopic scale (13, 14, 58, 67). Some of the models suffer from the assumption of purely elastic membrane, and are able

to capture only the RBC mechanical response, but cannot quantitatively represent realistic RBC rheology and dynamics. Fully continuum (fluid and solid) models often suffer from non-trivial coupling between nonlinear solid deformations and fluid flow with consequential computational expense. Therefore, “semi-continuum” models (15, 70) of deformable particles which use immersed boundary or front-tracking techniques are developing rapidly. In these, a membrane is represented by a set of points which are tracked in Lagrangian fashion and are coupled to an Eulerian discretization of fluid domain. These models employ the same external and internal fluids and do not take into account the existing viscosity contrast between them. In addition, continuum models omit some mesoscopic and microscopic scale phenomena such as membrane thermal fluctuations which affect RBC rheology and dynamics (57). On the microscopic scale, detailed spectrin molecular models of RBCs are much limited by the demanding computational expense. Therefore, we will focus here on an accurate mesoscopic modeling of red blood cells.

There exist several mesoscopic methods (13, 14, 58, 67) for modeling deformable particles such as RBCs. Dzwinel et al. (14) model RBCs as a volume of elastic material having an inner skeleton. This model does not take into account the main structural concept of red blood cell, namely a membrane filled with a fluid, and therefore it cannot capture properly the dynamics of RBCs, for example, the observed tumbling and tank-treading behavior in shear flow (1, 79). Three other aforementioned methods (13, 58, 67) employ a very similar approach to the method we will present here, where the RBC is represented by a network of springs in combination with bending rigidity and constraints for surface-area and volume conservation. Dupin et al. (13) couple the discrete RBC to a fluid described by the Lattice Boltzmann method (81). They obtained promising results, however the model does not consider external and internal fluids separation, membrane viscosity, and thermal fluctuations. Noguchi and Gompper (58) employed Multiparticle Collision Dynamics (51) and present encouraging results on vesicles and RBCs, however they do not use realistic RBC properties and probe only a single aspect of RBC dynamics. Pivkin and Karniadakis (67) used Dissipative Particle Dynamics (DPD) (40) for a multiscale RBC model which will be the basis of the general multiscale RBC (MS-RBC) model we will present here. The MS-RBC model is able to successfully capture RBC mechanics, rheology, and dynamics; this very accurate model was first published in (24). Potential membrane strain hardening or softening as well as the effects of metabolic activity can also be incorporated into the model leading to predictive capabilities on the progression of diseases such as malaria. Theoretical analysis of the hexagonal network yields its linear mechanical properties, and completely eliminates adjustment of the model parameters. Such models can be used to represent seamlessly the RBC membrane, cytoskeleton, cytosol, the surrounding plasma and even the parasite, e.g. in malaria-infected RBC, see figure 1. However, it is quite expensive computationally, and to this end, we also present a *low-dimensional* red blood cell model (LD-RBC), also based on DPD, that is more appropriate for blood flow simulations in large arterioles (60).

This chapter is organized as follows: In section two we review the basic DPD theory, the two RBC models, as well as aspects of the aggregation and adhesion

models that are especially important in modeling hematologic disorders. In section three we present some details on how we can use diverse single-cell static and dynamic measurements to estimate key macroscopic parameters, which upon mapping to the network (microscopic) parameters serve as input to the models. In section four we first present validation tests based on single-cell experiments. Subsequently, we present validation tests for whole blood, demonstrating that both models can predict the human blood viscosity in a wide range of shear rate values, including the low shear rate regime, where aggregation and rouleaux formation are responsible for the strong non-Newtonian blood behavior. In section five, we apply to malaria the framework we developed, i.e. from single-cell-measurements parameter estimation to predicting the mechanical and rheological behavior of infected blood in malaria. We conclude in section six with a brief summary and a discussion on the potential of multiscale modeling to predicting the state and evolution of hematologic disorders.

## 2 Methods and Models

We first review two formulations of the dissipative particle dynamics (DPD) method that we employ in modeling RBCs and blood flow. We then provide specific details on the multiscale RBC model (MS-RBC) and subsequently on the low-dimensional RBC model (LD-RBC), including the aggregation and adhesion models. Finally, we present details on the scaling from DPD units to physical units.

### 2.1 Dissipative Particle Dynamics: Original Method

Dissipative Particle Dynamics (DPD) (34, 40) is a mesoscopic particle method, where each particle represents a *molecular cluster* rather than an individual atom, and can be thought of as a soft lump of fluid. A first-principles derivation of the DPD method from the Liouville equation is presented in (45). The DPD system consists of  $N$  point particles of mass  $m_i$ , position  $\mathbf{r}_i$  and velocity  $\mathbf{v}_i$ . DPD particles interact through three forces: conservative ( $\mathbf{F}_{ij}^C$ ), dissipative ( $\mathbf{F}_{ij}^D$ ), and random ( $\mathbf{F}_{ij}^R$ ) forces given by

$$\begin{aligned}\mathbf{F}_{ij}^C &= F_{ij}^C(r_{ij})\hat{\mathbf{r}}_{ij}, \\ \mathbf{F}_{ij}^D &= -\gamma\omega^D(r_{ij})(\mathbf{v}_{ij} \cdot \hat{\mathbf{r}}_{ij})\hat{\mathbf{r}}_{ij}, \\ \mathbf{F}_{ij}^R &= \sigma\omega^R(r_{ij})\frac{\xi_{ij}}{\sqrt{dt}}\hat{\mathbf{r}}_{ij},\end{aligned}\tag{1}$$

where  $\hat{\mathbf{r}}_{ij} = \mathbf{r}_{ij}/r_{ij}$ , and  $\mathbf{v}_{ij} = \mathbf{v}_i - \mathbf{v}_j$ . The coefficients  $\gamma$  and  $\sigma$  define the strength of dissipative and random forces, respectively. In addition,  $\omega^D$  and  $\omega^R$  are weight functions, and  $\xi_{ij}$  is a normally distributed random variable with zero mean, unit variance, and  $\xi_{ij} = \xi_{ji}$ . All forces are truncated beyond the cutoff radius  $r_c$ , which defines the length scale in the DPD system. The conservative force is given by

$$F_{ij}^C(r_{ij}) = \begin{cases} a_{ij}(1 - r_{ij}/r_c) & \text{for } r_{ij} \leq r_c, \\ 0 & \text{for } r_{ij} > r_c, \end{cases} \quad (2)$$

where  $a_{ij}$  is the conservative force coefficient between particles  $i$  and  $j$ .

The random and dissipative forces form a thermostat and must satisfy the fluctuation-dissipation theorem in order for the DPD system to maintain equilibrium temperature  $T$  (18). This leads to:

$$\omega^D(r_{ij}) = [\omega^R(r_{ij})]^2, \quad \sigma^2 = 2\gamma k_B T, \quad (3)$$

where  $k_B$  is the Boltzmann constant. The choice for the weight functions is as follows

$$\omega^R(r_{ij}) = \begin{cases} (1 - r_{ij}/r_c)^k & \text{for } r_{ij} \leq r_c, \\ 0 & \text{for } r_{ij} > r_c, \end{cases} \quad (4)$$

where  $k = 1$  for the original DPD method. However, other choices (e.g.,  $k = 0.25$ ) for these envelopes have been used (21, 27) in order to increase the viscosity of the DPD fluid.

The time evolution of velocities and positions of particles is determined by the Newton's second law of motion

$$d\mathbf{r}_i = \mathbf{v}_i dt, \quad (5)$$

$$d\mathbf{v}_i = \frac{1}{m_i} \sum_{j \neq i} (\mathbf{F}_{ij}^C + \mathbf{F}_{ij}^D + \mathbf{F}_{ij}^R) dt. \quad (6)$$

The above stochastic equations of motion can be integrated using a modified velocity-Verlet algorithm (34); for systems governed by mixed hard-soft potentials sub-cycling techniques similar to the ones presented in (84) can be employed.

## 2.2 DPD Method for Colloidal Particles

To simulate colloidal particles by single DPD particles, we use a new formulation of DPD, in which the dissipative forces acting on a particle are explicitly divided into two separate components: *central* and *shear* (non-central) components. This allows us to redistribute and hence, balance the dissipative forces acting on a single particle to obtain the correct hydrodynamics. The resulting method was shown to yield the quantitatively correct hydrodynamic forces and torques on a single DPD particle (63), and thereby produce the correct hydrodynamics for colloidal particles (61). This formulation is reviewed below.

We consider a collection of particles with positions  $\mathbf{r}_i$  and angular velocities  $\Omega_i$ . We define  $\mathbf{r}_{ij} = \mathbf{r}_i - \mathbf{r}_j$ ,  $r_{ij} = |\mathbf{r}_{ij}|$ ,  $\mathbf{e}_{ij} = \mathbf{r}_{ij}/r_{ij}$ ,  $\mathbf{v}_{ij} = \mathbf{v}_i - \mathbf{v}_j$ . The force and torque on particle  $i$  are given by

$$\begin{aligned}\mathbf{F}_i &= \sum_j \mathbf{F}_{ij}, \\ \mathbf{T}_i &= -\sum_j \lambda_{ij} \mathbf{r}_{ij} \times \mathbf{F}_{ij}.\end{aligned}\quad (7)$$

Here, the factor  $\lambda_{ij}$  (introduced in (72)) is included as a weight to account for the different contributions from the particles in different species (solvent or colloid) differentiated in sizes while still conserving the angular momentum. It is defined as

$$\lambda_{ij} = \frac{R_i}{R_i + R_j}, \quad (8)$$

where  $R_i$  and  $R_j$  denote the radii of the particles  $i$  and  $j$ , respectively. The force exerted by particle  $j$  on particle  $i$  is given by

$$\mathbf{F}_{ij} = \mathbf{F}_{ij}^U + \mathbf{F}_{ij}^T + \mathbf{F}_{ij}^R + \tilde{\mathbf{F}}_{ij}. \quad (9)$$

The radial conservative force  $\mathbf{F}_{ij}^U$  can be that of standard DPD and is given in equation (2). The *translational force* is given by

$$\begin{aligned}\mathbf{F}_{ij}^T &= -[\gamma_{ij}^\perp f^2(r) \mathbf{1} + (\gamma_{ij}^\parallel - \gamma_{ij}^\perp) f^2(r) \mathbf{e}_{ij} \mathbf{e}_{ij}] \cdot \mathbf{v}_{ij} \\ &= -\gamma_{ij}^\parallel f^2(r_{ij}) (\mathbf{v}_{ij} \cdot \mathbf{e}_{ij}) \mathbf{e}_{ij} - \gamma_{ij}^\perp f^2(r_{ij}) [\mathbf{v}_{ij} - (\mathbf{v}_{ij} \cdot \mathbf{e}_{ij}) \mathbf{e}_{ij}].\end{aligned}\quad (10)$$

It accounts for the drag due to the relative translational velocity  $\mathbf{v}_{ij}$  of particles  $i$  and  $j$ . This force is decomposed into two components: one along and the other perpendicular to the lines connecting the centers of the particles. Correspondingly, the drag coefficients are denoted by  $\gamma_{ij}^\parallel$  and  $\gamma_{ij}^\perp$  for a “*central*” and a “*shear*” components, respectively. We note that the central component of the force is identical to the dissipative force of standard DPD (eq. (1)).

The *rotational force* is defined by

$$\mathbf{F}_{ij}^R = -\gamma_{ij}^\perp f^2(r_{ij}) [\mathbf{r}_{ij} \times (\lambda_{ij} \boldsymbol{\Omega}_i + \lambda_{ji} \boldsymbol{\Omega}_j)], \quad (11)$$

while the *random force* is given by

$$\tilde{\mathbf{F}}_{ij} dt = f(r_{ij}) \left[ \frac{1}{\sqrt{3}} \sigma_{ij}^\parallel \text{tr}[d\mathbf{W}_{ij}] \mathbf{1} + \sqrt{2} \sigma_{ij}^\perp d\mathbf{W}_{ij}^A \right] \cdot \mathbf{e}_{ij}, \quad (12)$$

where  $\sigma_{ij}^\parallel = \sqrt{2k_B T \gamma_{ij}^\parallel}$  and  $\sigma_{ij}^\perp = \sqrt{2k_B T \gamma_{ij}^\perp}$  are chosen to satisfy the fluctuation-dissipation theorem,  $d\mathbf{W}_{ij}$  is a matrix of independent Wiener increments, and  $d\mathbf{W}_{ij}^A$  is defined as  $d\mathbf{W}_{ij}^{A\mu\nu} = \frac{1}{2}(d\mathbf{W}_{ij}^{\mu\nu} - d\mathbf{W}_{ij}^{\nu\mu})$ . We can also use the generalized weight function  $f(r) = (1 - \frac{r}{r_c})^k$  as in the previous section with  $k = 0.25$  (22) in equations (10)- (12). The numerical results in previous studies (62, 63) showed higher accuracy with  $k = 0.25$  compared to the usual choice  $k = 1$ . The standard DPD is recovered when  $\gamma_{ij}^\perp \equiv 0$ , i.e., when the “*shear*” components of the forces are ignored.

Colloidal particles are simulated as single DPD particles, similarly to the solvent particles but of larger size. The particle size can be adjusted with the coefficient  $a_{ij}$  of the conservative force (see eq. (2)). However, the standard linear force in DPD defined in eq. (2) is too soft to model any hard-sphere type of particles. To resolve this problem, we adopt an exponential conservative force for the colloid-colloid and colloid-solvent interactions, but keep the conventional DPD linear force for the solvent-solvent interactions. We have found that these hybrid conservative interactions produced colloidal particles dispersed in solvent without overlap, which was quantified by calculating the radial distribution function of colloidal particles (61). Moreover, the timestep is not significantly decreased, in contrast to the small timesteps required for the Lennard-Jones potential (72). The radial exponential conservative force is defined as

$$F_{ij}^U = \frac{a_{ij}}{1 - e^{b_{ij}}} (e^{b_{ij}r_{ij}/r_c^e} - e^{b_{ij}}), \quad (13)$$

where  $a_{ij}$  and  $b_{ij}$  are adjustable parameters, and  $r_c^e$  is its cutoff radius. The size of a colloidal particle can thus be controlled by adjusting the value of  $a_{ij}$  in eq. (13).

### 2.3 Multiscale Red Blood Cell (MS-RBC) Model

Here, we will use the DPD formulation described in section 2.1. The average equilibrium shape of a RBC is biconcave as measured experimentally (20), and is represented by

$$z = \pm D_0 \sqrt{1 - \frac{4(x^2 + y^2)}{D_0^2}} \left[ a_0 + a_1 \frac{x^2 + y^2}{D_0^2} + a_2 \frac{(x^2 + y^2)^2}{D_0^4} \right], \quad (14)$$

where  $D_0 = 7.82 \mu\text{m}$  is the average diameter,  $a_0 = 0.0518$ ,  $a_1 = 2.0026$ , and  $a_2 = -4.491$ . The surface area and volume of this RBC are equal to  $135 \mu\text{m}^2$  and  $94 \mu\text{m}^3$ , respectively.

In simulations, the membrane network structure is generated by triangulating the unstressed equilibrium shape described by (14). The cell shape is first imported into a grid generator to produce an initial triangulation based on the advancing-front method. Subsequently, free-energy relaxation is performed by flipping the diagonals of quadrilateral elements formed by two adjacent triangles, while the vertices are constrained to move on the prescribed surface. The relaxation procedure includes only elastic in-plane and bending energy components described below.

Figure 2 shows the membrane model represented by a set of points  $\{\mathbf{x}_i\}$ ,  $i \in 1 \dots N_v$  that are the vertices of a two-dimensional triangulated network on the RBC surface described by equation (14). The vertices are connected by  $N_s$  edges which form  $N_t$  triangles. The potential energy of the system is defined as follows

$$V(\{\mathbf{x}_i\}) = V_{in-plane} + V_{bending} + V_{area} + V_{volume}. \quad (15)$$

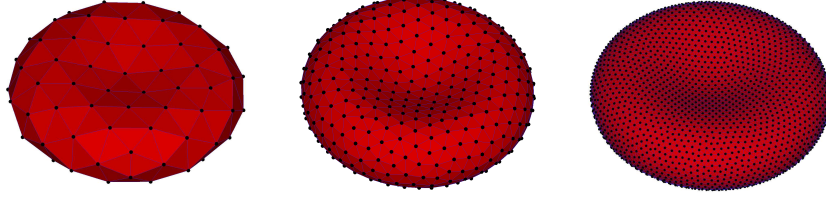


**Fig. 2** MS-RBC membrane model with  $N_v = 100, 500,$  and  $3000$  from left to right, respectively.

The in-plane elastic energy mimics the elastic spectrin network, and is given by

$$V_{in-plane} = \sum_{j \in 1 \dots N_s} \left[ \frac{k_B T l_m (3x_j^2 - 2x_j^3)}{4p(1-x_j)} + \frac{k_p}{(n-1)l_j^{n-1}} \right], \quad (16)$$

where  $l_j$  is the length of the spring  $j$ ,  $l_m$  is the maximum spring extension,  $x_j = l_j/l_m$ ,  $p$  is the persistence length,  $k_B T$  is the energy unit,  $k_p$  is the spring constant, and  $n$  is a power. Note that the spring forces in membrane are a combination of conservative elastic forces, that may be expressed in terms of the energy potential above, and dissipative forces to be defined below. The first term in (16) corresponds to the attractive wormlike chain (WLC) potential, and the second term defines a repulsive force for  $n > 0$  to be called the power force (POW), so that we abbreviate this spring model as WLC-POW. Note that if  $n = 1$  the power force energy should be defined as  $-k_p \log(l_j)$ . A non-zero equilibrium spring length is defined by the balance of these two forces.

The bending energy represents the bending resistance of the lipid bilayer and is defined as

$$V_{bending} = \sum_{j \in 1 \dots N_s} k_b [1 - \cos(\theta_j - \theta_0)], \quad (17)$$

where  $k_b$  is the bending constant,  $\theta_j$  is the instantaneous angle between two adjacent triangles having the common edge  $j$ , and  $\theta_0$  is the spontaneous angle. The above bending energy is a discretization (76) of the macroscopic Helfrich model (36).

The area and volume conservation constraints which account for area-incompressibility of the lipid bilayer and incompressibility of the inner cytosol, respectively, are expressed as

$$V_{area} = \frac{k_a (A - A_0^{tot})^2}{2A_0^{tot}} + \sum_{j \in 1 \dots N_t} \frac{k_d (A_j - A_0)^2}{2A_0}, \quad (18a)$$

$$V_{volume} = \frac{k_v (V - V_0^{tot})^2}{2V_0^{tot}}, \quad (18b)$$

where  $k_a$ ,  $k_d$  and  $k_v$  are the global area, local area and volume constraint coefficients, respectively. The terms  $A$  and  $V$  are the total area and volume of RBC, while  $A_0^{tot}$  and  $V_0^{tot}$  are the specified total area and volume, respectively. Note that the above expressions define global area and volume constraints, and the second term

in equation (18a) incorporates the local dilatation constraint. Detailed description and discussion of the RBC model can be found in (24, 25).

Particle forces are derived from the above energies as follows

$$\mathbf{f}_i = -\partial V(\{\mathbf{x}_i\})/\partial \mathbf{x}_i, \quad i \in 1 \dots N_p. \quad (19)$$

Exact force expressions can be found in (23).

### 2.3.1 Mechanical Properties

Linear analysis of the regular hexagonal network having the above energies yields a relationship between macroscopic elastic properties (shear, area-compression, and Young's moduli) of the network and model parameters (24, 25). The membrane shear modulus is thus given by

$$\mu_0 = \frac{\sqrt{3}k_B T}{4\rho l_m x_0} \left( \frac{x_0}{2(1-x_0)^3} - \frac{1}{4(1-x_0)^2} + \frac{1}{4} \right) + \frac{\sqrt{3}k_p(n+1)}{4l_0^{n+1}}, \quad (20)$$

where  $l_0$  is the equilibrium spring length and  $x_0 = l_0/l_m$ . The corresponding area-compression and Young's moduli are found as follows

$$K_0 = 2\mu_0 + k_a + k_d, \quad Y_0 = \frac{4K_0\mu_0}{K_0 + \mu_0}. \quad (21)$$

The bending coefficient  $k_b$  of equation (17) can be expressed in terms of the macroscopic bending rigidity  $k_c$  of the Helfrich model (36) as  $k_b = 2k_c/\sqrt{3}$ .

### 2.3.2 Membrane Viscoelasticity

The above model defines a purely elastic membrane, however the RBC membrane is known to be viscoelastic. To incorporate viscosity into the model, the spring definition is modified by adding viscous contribution through dissipative and random forces. Such a term fits naturally in the DPD method (40), where inter-particle dissipative interactions are an intrinsic part of the method. Straightforward implementation of the dissipative interactions as  $\mathbf{F}_{ij}^D = -\gamma(\mathbf{v}_{ij} \cdot \mathbf{e}_{ij})\mathbf{e}_{ij}$  ( $\gamma$  is the dissipative parameter,  $\mathbf{v}_{ij} = \mathbf{v}_i - \mathbf{v}_j$  is the relative velocity of vertices  $i$  and  $j$  connected by a spring, and  $\mathbf{e}_{ij}$  is the direction along the spring with unit length) appears to be insufficient. Experience shows that small  $\gamma$  results in a negligible viscous contribution since  $\mathbf{v}_{ij} \cdot \mathbf{e}_{ij} \sim 0$ , while large values of  $\gamma$  require considerably smaller time steps to overcome the numerical instability. Better performance is achieved with a viscous spring dissipation term  $-\gamma\mathbf{v}_{ij}$ , which is similar to a ‘‘dashpot’’, and in combination with a spring force represents the Kelvin-Voigt model of a viscoelastic spring. For this term the fluctuation-dissipation balance needs to be imposed to ensure the maintenance of the equilibrium membrane temperature  $k_B T$ . We follow the

general framework of the fluid particle model (17), and define  $\mathbf{F}_{ij}^D = -\mathbf{T}_{ij} \cdot \mathbf{v}_{ij}$  and  $\mathbf{T}_{ij} = \gamma^T \mathbf{1} + \gamma^C \mathbf{e}_{ij} \mathbf{e}_{ij}$ , where  $\gamma^T$  and  $\gamma^C$  are the dissipative coefficients. This definition results in the dissipative interaction term of the kind

$$\mathbf{F}_{ij}^D = -[\gamma^T \mathbf{1} + \gamma^C \mathbf{e}_{ij} \mathbf{e}_{ij}] \cdot \mathbf{v}_{ij} = -\gamma^T \mathbf{v}_{ij} - \gamma^C (\mathbf{v}_{ij} \cdot \mathbf{e}_{ij}) \mathbf{e}_{ij}, \quad (22)$$

where the second term is analogous to the dissipative force in DPD. From the fluctuation-dissipation theorem, random interactions are given by

$$\mathbf{F}_{ij}^R dt = \sqrt{2k_B T} \left( \sqrt{2\gamma^T} d\overline{\mathbf{W}}_{ij}^S + \sqrt{3\gamma^C - \gamma^T} \frac{tr[d\mathbf{W}_{ij}]}{3} \mathbf{1} \right) \cdot \mathbf{e}_{ij}, \quad (23)$$

where  $tr[d\mathbf{W}_{ij}]$  is the trace of a random matrix of independent Wiener increments  $d\mathbf{W}_{ij}$ , and  $d\overline{\mathbf{W}}_{ij}^S = d\mathbf{W}_{ij}^S - tr[d\mathbf{W}_{ij}^S] \mathbf{1}/3$  is the traceless symmetric part, while  $d\mathbf{W}_{ij}^S = [d\mathbf{W}_{ij} + d\mathbf{W}_{ij}^T]/2$  is the symmetric part. Note, that the last equation imposes the condition  $3\gamma^C > \gamma^T$ . The defined dissipative and random forces in combination with an elastic spring constitute a viscoelastic spring whose equilibrium temperature  $k_B T$  is constant. To relate the membrane shear viscosity  $\eta_m$  and the dissipative parameters  $\gamma^T$ ,  $\gamma^C$  we employ the idea used for the derivation of membrane elastic properties (see (23, 24) for details) and obtain the following relation

$$\eta_m = \sqrt{3} \gamma^T + \frac{\sqrt{3} \gamma^C}{4}. \quad (24)$$

Clearly,  $\gamma^T$  accounts for a large portion of viscous contribution, and therefore  $\gamma^C$  is set to  $\gamma^T/3$  in all simulations.

### 2.3.3 RBC-Solvent Boundary Conditions

The RBC membrane encloses a volume of fluid and is itself suspended in a solvent. In particle methods, such as DPD, fluids are represented as a collection of interacting particles. Thus, in order to impose appropriate boundary conditions (BCs) between the membrane and the external/internal fluids two matters need to be addressed:

- i) enforcement of membrane impenetrability to prevent mixing of the inner and the outer fluids,
- ii) no-slip BCs imposed through pairwise point interactions between the fluid particles and the membrane vertices.

Membrane impenetrability is enforced by imposing bounce-back reflection of fluid particles at the moving membrane triangular plaquettes. The bounce-back reflection enhances the no-slip boundary conditions at the membrane surface as compared to specular reflection; however, it does not guarantee no-slip. Additional dissipation enhancement between the fluid and the membrane is required to achieve no-slip at the membrane boundary. For this purpose, the DPD dissipative force between fluid particles and membrane vertices needs to be properly set based on the

idealized case of linear shear flow over a flat plate. In continuum, the total shear force exerted by the fluid on the area  $A$  is equal to  $A\eta\dot{\gamma}$ , where  $\eta$  is the fluid's viscosity and  $\dot{\gamma}$  is the local wall shear-rate. In DPD, we distribute a number of particles on the wall to mimic the membrane vertices. The force on a single wall particle exerted by the sheared fluid can be found as follows

$$F_v = \int_{V_h} n g(r) F^D dV, \quad (25)$$

where  $F^D$  is the DPD dissipative force (17) between fluid particles and membrane vertices,  $n$  is the fluid number density,  $g(r)$  is the radial distribution function of fluid particles with respect to the wall particles, and  $V_h$  is the half sphere volume of fluid above the wall. Here, the total shear force on the area  $A$  is equal to  $N_A F_v$ , where  $N_A$  is the number of wall particles enclosed by  $A$ . The equality of  $N_A F_v = A\eta\dot{\gamma}$  results in an expression of the dissipative force coefficient in terms of the fluid density and viscosity, and the wall density  $N_A/A$ , while under the assumption of linear shear flow the shear rate  $\dot{\gamma}$  cancels out. This formulation results in satisfaction of the no-slip BCs for the linear shear flow over a flat plate. It also serves as an excellent approximation for no-slip at the membrane surface in spite of the assumptions made. Note that in the absence of conservative interactions between fluid and wall particles  $g(r) = 1$ .

### 2.3.4 RBC Aggregation Interactions

For a blood suspension the attractive cell-cell interactions are crucial for simulation of aggregation into rouleaux. These forces are approximated phenomenologically with the Morse potential given by

$$\phi(r) = D_e \left[ e^{2\beta(r_0-r)} - 2e^{\beta(r_0-r)} \right], \quad (26)$$

where  $r$  is the separation distance,  $r_0$  is the zero force distance,  $D_e$  is the well depth of the potential, and  $\beta$  characterizes the interaction range. For the MS-RBC model the Morse potential interactions are implemented between every two vertices of separate RBCs if they are within a defined potential cutoff radius  $r_M$  as shown in figure 3. The Morse interactions consist of a short-range repulsive force when  $r < r_0$  and of a long-range attractive force for  $r > r_0$ . However, such repulsive interactions cannot prevent two RBCs from an overlap. To guarantee no overlap among RBCs we employ a short range Lennard-Jones potential and specular reflections of RBC vertices on membranes of other RBCs. The Lennard-Jones potential is defined as

$$U_{LJ}(r) = 4\epsilon \left[ \left( \frac{\sigma_{LJ}}{r} \right)^{12} - \left( \frac{\sigma_{LJ}}{r} \right)^6 \right], \quad (27)$$

where  $\epsilon$  and  $\sigma_{LJ}$  are energy and length characteristic parameters, respectively. These interactions are repulsive and vanish beyond  $r > 2^{1/6}\sigma_{LJ}$ . In addition, specular re-



**Fig. 3** Aggregation interactions for the MS-RBC model.

flexions of RBC vertices on surfaces of other RBCs are necessary due to coarseness of the triangular network, which represents the RBC membrane.

### 2.3.5 RBC Adhesion Interactions

Adhesion of Pf-RBCs to coated surfaces is mediated by the interactions between receptors and ligands which are the adhesion sites distributed on a cell and a surface, respectively. A potential bond between a receptor and a ligand may be formed only if the receptor is close enough to the free ligand, which is characterized by the reactive distance  $d_{on}$ . A ligand is called free if it is not bound to any receptors. During the time a receptor is within the distance  $d_{on}$  to a free ligand, a bond can be formed with on-rate  $k_{on}$ . Reversely, existing bonds are ruptured with off-rate  $k_{off}$  or if their length exceeds the rupture distance  $d_{off}$ . The rates  $k_{on}$  and  $k_{off}$  are defined as follows

$$k_{on} = k_{on}^0 \exp\left(-\frac{\sigma_{on}(l-l_0)^2}{2k_B T}\right), \quad k_{off} = k_{off}^0 \exp\left(\frac{\sigma_{off}(l-l_0)^2}{2k_B T}\right), \quad (28)$$

where  $k_{on}^0$  and  $k_{off}^0$  are the reaction rates at the distance  $l = l_0$  between a receptor and a ligand with the equilibrium spring length  $l_0$  defined below. The effective on and off strengths  $\sigma_{on}$  and  $\sigma_{off}$  define a decrease or an increase of the corresponding rates within the interaction lengths  $d_{on}$  and  $d_{off}$ , and  $k_B T$  is the unit of energy. The force exerted on the receptors and ligands by an existing bond is given by

$$F(l) = k_s(l - l_0), \quad (29)$$

where  $k_s$  is the spring constant. The probabilities of bond formation and dissociation are defined as  $P_{on} = 1 - \exp(-k_{on}\Delta t)$  and  $P_{off} = 1 - \exp(-k_{off}\Delta t)$ , where  $\Delta t$  is the time step in simulations. This adhesion model is a slight modification of the well-known adhesive dynamics model developed by Hammer and Apte (35) primarily for

leukocytes. In their model  $\sigma_{on} = \sigma_{ts}$  and  $\sigma_{off} = k_s - \sigma_{ts}$ , where  $\sigma_{ts}$  is the transition state spring constant.

During the course of a simulation the receptor/ligand interactions are considered every time step. First, all existing bonds between receptors and ligands are checked for a potential dissociation according to the probability  $P_{off}$ . A bond is ruptured if  $\xi < P_{off}$  and left unchanged otherwise, where  $\xi$  is a random variable uniformly distributed on  $[0, 1]$ . If a bond is ruptured the corresponding ligand is available for new binding. Second, all free ligands are examined for possible bond formations. For each free ligand we loop over the receptors within the distance  $d_{on}$ , and bond formation is attempted for each found receptor according to the probability  $P_{on}$ . This loop is terminated when a bond is formed. Finally, the forces of all remaining bonds are calculated and applied.

Note that this algorithm permits only a single bond per ligand, while receptors may establish several bonds if several ligands are free within their reaction radius. This provides an additional capability for the adhesive dynamics model compared with that employing one-to-one interactions between receptors and ligands. Also, this assumption appears to furnish a more realistic representation of adhesive interactions of Pf-RBCs with a coated surface. Pf-RBCs display a number of parasitic nanometer-size protrusions or knobs on the membrane surface (39, 41, 55), where receptors that mediate RBC adherence are clustered.

## 2.4 Low-Dimensional RBC (LD-RBC) Model

Here, we will employ the DPD formulation presented in section 2.2. The LD-RBC is modeled as a ring of 10 colloidal DPD particles connected by wormlike chain (WLC) springs. The intrinsic size of colloidal particle is determined by the radius of the sphere effectively occupied by a single DPD particle (61), which is defined by the distribution of its surrounding solvent particles.

To construct the cell model, however, we allow particles in the same RBC to overlap, i.e., the colloidal particles in the same cell still interact with each other through the soft standard DPD linear force (see eq. (2)). The radius,  $a$ , of each colloidal particle is chosen to be equal to the radius of the ring, and hence the configuration of RBC is approximately a closed-torus as shown in figure 4.

The WLC spring force interconnecting all cell particles in each RBC is given by

$$F_{WLC}^U = \frac{k_B T}{p} \left[ \frac{1}{4 \left(1 - \frac{r_{ij}}{l_m}\right)^2} - \frac{1}{4} + \frac{r_{ij}}{l_m} \right], \quad (30)$$

where  $r_{ij}$  is the distance between two neighboring beads,  $p$  is the persistence length, and  $l_m$  is the maximum allowed length for each spring. Since the cell has also bending resistance, we incorporate into the ring model bending resistance in the form of ‘‘angle’’ bending forces dependent on the angle between two consecutive springs. The bending forces are derived from the cosine bending potential given by

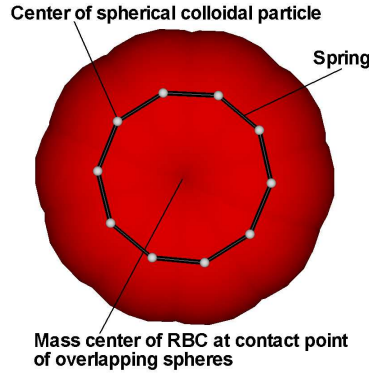


**Fig. 4** LD-RBC: A sketch of the low-dimensional closed-torus like RBC model.

$$U_{ijk}^{COS} = k_b[1 - \cos\theta_{ijk}], \quad (31)$$

where  $k_b$  is the bending stiffness, and  $\theta_{ijk}$  is the angle between two consecutive springs.

Here,  $p$  determines the Young's modulus, and along with  $l_m$  and  $a$  give the right size of RBC. To match both axial and transverse RBC deformations with the experimental data (82),  $k_b$  is adjusted to reach a good agreement, which also gives some contribution to the Young's modulus. The LD-RBC model does not have the membrane shear modulus.

Since the thickness of LD-RBC model is constant, we estimate the variations of the RBC volume and surface area under stretching by calculating the relative change of the area formed by the ring under stretching. For healthy RBCs we find that it varies within only 8% in the range of all stretching forces (60). Therefore, the surface-area and hence the volume of RBCs remain approximately constant in the LD-RBC model.

#### 2.4.1 Number of Particles in LD-RBC Model

We examine the effect of coarse-graining on stretching response by varying the number of particles ( $N_c$ ) to model the LD-RBC. Figure 5 shows the RBC shape evolution from equilibrium (0  $pN$  force) to 100  $pN$  stretching force at different  $N_c$ . Note that an increase of the number of particles making up the RBC results in a smoother RBC surface. However, this feature seems to be less pronounced for higher  $N_c$ . Also, when we stretch the RBCs with different  $N_c$ , we find that an increase of  $N_c$  results in better agreement with the experimental data (82), but after  $N_c = 10$ , the change becomes very small (60). To gain sufficiently good agreement and keep the computation cost low, we choose  $N_c = 10$  for all the simulations shown herein; this is the accurate minimalistic model that we employ in our studies.

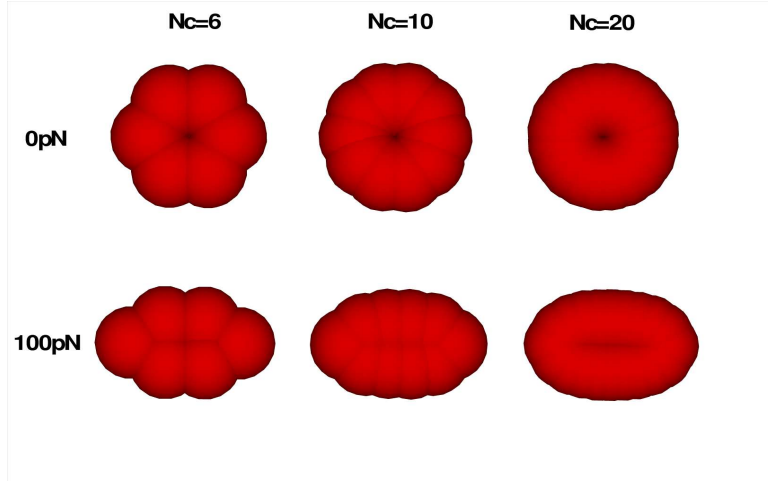


**Fig. 5** LD-RBC shape evolution at different  $N_c$  (number of particles in LD-RBC model) and stretching forces.

#### 2.4.2 Aggregation Model

For LD-RBC model, we also employ the Morse potential, see equation (26), to model the total intercellular attractive interaction energy. The interaction between RBCs derived from the Morse potential includes two parts: a short-ranged repulsive force and a weak long-ranged attractive force. The repulsive force is in effect when the distance between two RBC surfaces is  $r < r_0$ , where  $r_0$  is usually in nanometer scale (7, 48, 56). In our simulations,  $r_0$  is chosen to be  $200nm$ .

Here,  $r$  is calculated based on the center of mass of RBCs, i.e.,  $r$  is equal to the distance between the center of mass of two RBCs minus the thickness of a RBC. We also calculate the normal vector of each RBC ( $\mathbf{n}_c$ ), which is used to determine if the aggregation occurs between two RBCs according to the angles formed by the normal vectors of two RBCs with their center line. The RBC normal vector is defined as

$$\mathbf{n}_c = \frac{\sum \mathbf{v}_k \times \mathbf{v}_{k+1}}{N_c}, \mathbf{v}_k = \mathbf{x}_k - \mathbf{x}_c. \quad (32)$$

Here,  $\mathbf{x}_k$  is the position of the  $k$ th particle in each RBC,  $\mathbf{x}_c$  is the position of the center of mass, and  $N_c$  is the number of particles in each RBC. The center line  $\mathbf{v}_{cij}$  of two RBCs (cell  $i$  and cell  $j$ ) is defined as  $\mathbf{x}_{ci} - \mathbf{x}_{cj}$ . The angle formed by the normal vector of one cell with the center line is determined by their dot product

$$d_i = \frac{\mathbf{n}_{ci} \cdot \mathbf{v}_{cij}}{\|\mathbf{n}_{ci}\| \cdot \|\mathbf{v}_{cij}\|}. \quad (33)$$

The Morse interaction is turned on if  $d_i > d_c$  and  $d_j > d_c$ , otherwise, it is kept off. The critical value,  $d_c$ , is chosen to be equal to  $\cos(\pi/4)$ , i.e., the critical angle ( $\theta_c$ )

to turn on/off the aggregation interaction is  $\pi/4$ . This value is found to be suitable to induce rouleaux formation, but exclude the disordered aggregation. The proposed aggregation algorithm can be further illustrated by a sketch in figure 6, where the aggregation between two neighbor RBCs is decided to be on/off according to their relative orientation.

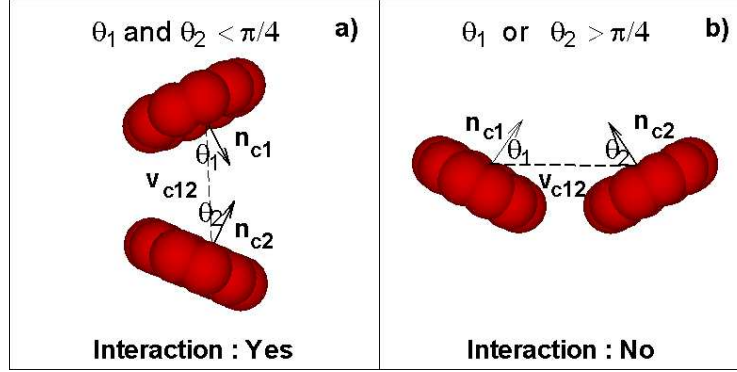


**Fig. 6** Schematic of the aggregation algorithm. Here, the two neighbor RBCs (1 and 2) are to aggregate or not if the angles,  $\theta_1$  and  $\theta_2$ , are smaller or greater than  $\pi/4$ .

## 2.5 Scaling of Model and Physical Units

The dimensionless constants and variables in the DPD model must be scaled with physical units. The superscript  $M$  denotes that a quantity is in “model” units, while  $P$  identifies physical units (SI units). We define the length scale as follows

$$r^M = \frac{D_0^P}{D_0^M} m, \quad (34)$$

where  $r^M$  is the model unit of length,  $D_0$  is the cell diameter, and  $m$  stands for meters. The energy per unit mass ( $k_B T$ ) and the force unit (“ $N$ ” denotes Newton) scales are given by

$$(k_B T)^M = \frac{Y^P}{Y^M} \left( \frac{D_0^P}{D_0^M} \right)^2 (k_B T)^P, \quad N^M = \frac{Y^P}{Y^M} \frac{D_0^P}{D_0^M} N^P, \quad (35)$$

where  $Y$  is the membrane Young’s modulus. The time scale is defined as

$$\tau = \frac{D_0^P}{D_0^M} \frac{\eta^P}{\eta^M} \frac{Y^M}{Y^P} s, \quad (36)$$

where  $\eta$  is a characteristic viscosity (e.g., solvent or membrane).

### 3 Parameter Estimation

The models described in the previous section require as inputs “microscopic” parameters, e.g. the persistence length  $p$  for the WLC potential, but also other parameters, e.g. values of the membrane viscosity. These parameters may not be readily available in the literature and certainly they vary according to the RBC state, i.e. a healthy or infected RBC. To this end, we aim to estimate most of the required parameters from single-cell measurements of macroscopic quantities, e.g. shear modulus, which can then be mapped to “microscopic” (network) parameters using analytical expressions, such as the one in equation (20). Specifically, the RBC model is compared against several available experiments which examine cell mechanics, rheology, and dynamics for healthy and diseased RBCs. First, we obtain the shear modulus using optical tweezers measurements of a stretched RBC. We then estimate the membrane rheological parameters using measurements from optical magnetic twisting cytometry and from the response of single RBC in shear flow. In all cases we run corresponding DPD simulations in order to compare and match the experimentally observed responses. In the following, we describe details of this procedure and we also demonstrate that while the parameters can be estimated in a relatively narrow regime, we can then predict accurately the single RBC mechanics, dynamics and rheology over a much wider range of operating conditions.

#### 3.1 Shear Modulus Using Optical Tweezers

To mimic the optical tweezers experiments of (82) a modeled RBC undergoes stretching by applying a stretching force on both ends of the cell. The total stretching force  $f^M$  is applied to  $N_-$  and  $N_+$  vertices ( $N_- = N_+ = \varepsilon N_v$ ) along the negative and the positive directions, respectively. These vertices cover a near-spherical area on the RBC surface with  $\varepsilon = 0.02$  which corresponds to the contact diameter of the attached silica bead with diameter  $2 \mu m$  used in experiments (82). Note that the viscous properties of the membrane and of the suspending medium do not affect final stretching since the RBC response is measured after convergence to the equilibrium stretched state is achieved for given force.

Figure 7 (left) compares the simulated axial and transverse RBC diameters with their experimental counterparts (82) for different coarse-graining levels starting from the spectrin-level ( $N_v = 27344$ ) to the highly coarse-grained network of  $N_v = 500$ . Excellent correspondence between simulations and experiments is achieved for  $\mu_0 = 6.3 \mu N/m$  and  $Y = 18.9 \mu N/m$  independently of the level of coarse-graining. The small discrepancy between simulated and experimental transverse diameters is probably a consequence of the optical measurements being per-

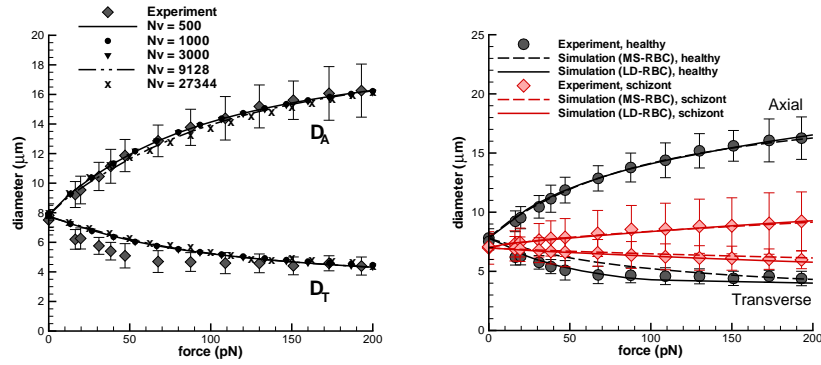


**Fig. 7** MS-RBC (left): Stretching response of a healthy RBC for different coarse-graining levels. MS-RBC vs. LD-RBC (right): Stretching response of a healthy RBC and a Pf-RBC (schizont stage) with the experiments of (82).  $D_A$  and  $D_T$  refer to the axial and transverse diameters. (From (23, 59)).

formed from only a single observation angle. Numerical simulations showed that RBCs subjected to stretching tend to rotate in  $y$ - $z$  plane, and therefore measurements from a single observation angle may result in underprediction of the maximum transverse diameter. However, the simulation results remain within the experimental error bars.

Next, we compare the MS-RBC versus the LD-RBC models; figure 7 (right) presents the axial and transverse RBC deformations for a healthy RBC and for a RBC at the latest stage (schizont) of intra-erythrocytic parasite development in malaria disease in comparison with experiments (82). Simulation results are in excellent agreement with the experiments for both RBC models. The Young's modulus of a RBC is found to be 18.9 and 180.0  $\mu N/m$  for healthy RBC and at the schizont stage, respectively, in case of the MS-RBC model, while the LD-RBC model yields the values of 20.0 and 199.5  $\mu N/m$  for the RBC Young's modulus. Note that the low-dimensional RBC model is able to capture linear as well as non-linear RBC elastic response.

### 3.2 Membrane Rheology from Twisting Torque Cytometry

Twisting torque cytometry (TTC) is the numerical analog of the optical magnetic twisting cytometry (OMTC) used in the experiments (52, 54), where a ferrimagnetic microbead is attached to RBC top and is subjected to an oscillating magnetic field. In simulations a microbead is attached to the modeled membrane, and is subjected to an oscillating torque as shown in figure 8 (left). In analogy with the experiments, the modeled RBC is attached to a solid surface, where the wall-adhesion is modeled by keeping stationary fifteen percent of vertices on the RBC bottom, while other

vertices are free to move. The adhered RBC is filled and surrounded by fluids having viscosities much smaller than the membrane viscosity, and therefore, only the membrane viscous contribution is measured. The microbead is simulated by a set of vertices on the corresponding sphere subject to a rigid body motion. The bead attachment is modeled by including several RBC vertices next to the microbead bottom into the rigid motion.

A typical bead response to an oscillating torque measured in simulations is given in figure 8 (right). The bead displacement has the same oscillating frequency as the

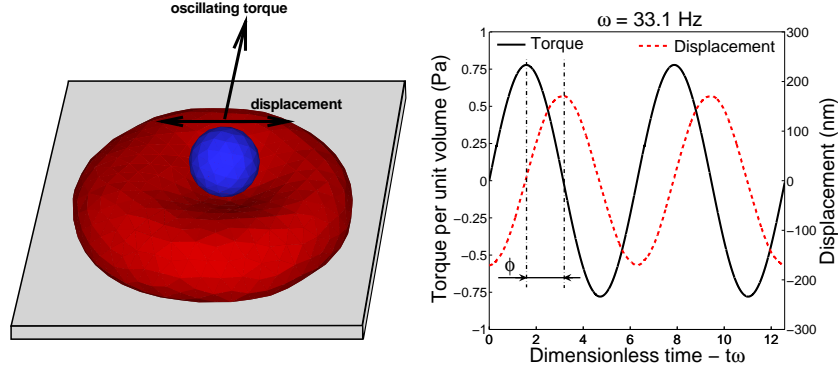


**Fig. 8** Setup of the TTC (left) and the characteristic response of a microbead subjected to an oscillating torque (right).

applied torque per unit volume, but it is shifted by a phase angle  $\phi$  depending on the frequency. The phase angle can be used to derive components of the complex modulus according to linear rheology as follows

$$g'(\omega) = \frac{\Delta T}{\Delta d} \cos(\phi), \quad g''(\omega) = \frac{\Delta T}{\Delta d} \sin(\phi), \quad (37)$$

where  $g'(\omega)$  and  $g''(\omega)$  are the *two-dimensional* storage and loss moduli ( $G'$  and  $G''$  in 3D), and  $\Delta T$  and  $\Delta d$  are the torque and bead displacement amplitudes. Note that under the assumption of no inertial effects, the phase angle satisfies the condition  $0 \leq \phi < \pi/2$ .

Figure 9 presents components of the complex modulus for healthy RBCs compared with experimental data of (54). A good agreement of the membrane moduli in simulations with the experimental data is found for the bending rigidity  $k_c = 4.8 \times 10^{-19} J$  and the membrane viscosity  $\eta_m = 0.022 Pa \cdot s$ . Note that this corresponds to the bending rigidity twice larger than the widely accepted value of  $2.4 \times 10^{-19} J$ . In figure 9 only the membrane bending rigidity is varied since the Young's modulus was obtained in the RBC stretching tests above. In summary, TTC for healthy RBCs revealed that the storage modulus ( $g'$ ) depends on the membrane

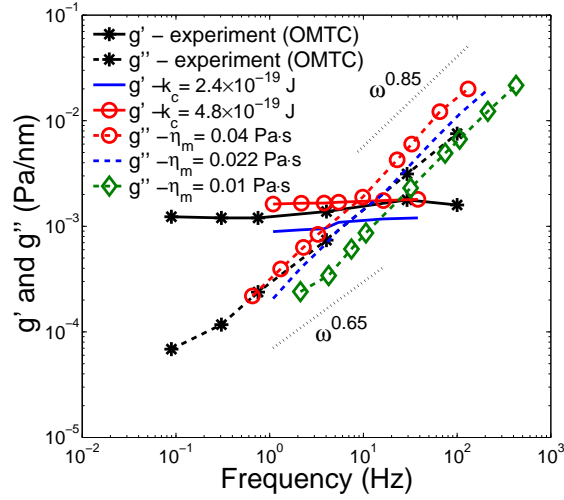


**Fig. 9** Two-dimensional storage and loss ( $g'$  and  $g''$ ) moduli of the RBC membrane obtained from simulations for different membrane viscosities and bending rigidities in comparison with the experiments (54). (From (23)).

elastic properties and bending rigidity, while the loss modulus ( $g''$ ) is governed by the membrane viscosity.

### 3.3 RBC Dynamics in Shear Flow

Experimental observations (1, 29, 30, 86) of RBC dynamics in shear flow show RBC tumbling at low shear rates and tank-treading at high shear rates. This behavior is related to existence of a RBC minimum energy state shown in the experiments by Fischer (29), where a RBC relaxed to its original state marked by several attached microbeads after some time of tank-treading motion. Hence, the RBC has to exceed a certain energy barrier in order to transit into a tank-treading motion in shear flow.

Theoretical predictions (1, 79) attempt to capture RBC dynamics in shear flow depending on the shear rate and the viscosity contrast defined as  $\lambda = (\eta_i + \eta_m)/\eta_o$ . According to the theories, for a small  $\lambda < 3$  a RBC tumbles at low shear rates and tank-treads at high shear rates. Near the tumbling-to-tank-treading transition there exists a narrow intermittent region where theories predict an instability such that RBC tumbling can be followed by tank-treading and vice versa. However, in case of a large viscosity contrast ( $\lambda > 3$ ) the theories predict a well-defined tumbling regime followed by an intermittent region, while stable tank-treading may not be present. In addition, the tank-treading state is also characterized by RBC swinging around the tank-treading axes with certain frequency and amplitude.

A simulated RBC is suspended into a solvent placed between two parallel walls moving with constant velocities in opposite directions. Figure 10 (left) shows tumbling and tank-treading frequencies with respect to shear rates in comparison with experiments (30, 86). Comparison of the simulated dynamics with experiments

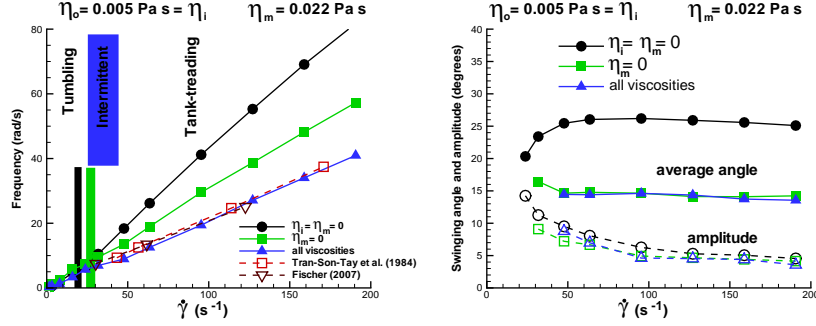


**Fig. 10** Tumbling and tank-treading frequency (left) of a RBC in shear flow and swinging average angle and amplitude (right) for different cases: 1)  $\eta_o = 5 \times 10^{-3} Pa \cdot s$ ,  $\eta_i = \eta_m = 0$  (circles); 2)  $\eta_o = \eta_i = 5 \times 10^{-3} Pa \cdot s$ ,  $\eta_m = 0$  (squares); 3)  $\eta_o = \eta_i = 5 \times 10^{-3} Pa \cdot s$ ,  $\eta_m = 22 \times 10^{-3} Pa \cdot s$  (triangles). (From (23)).

showed that a purely elastic RBC with or without inner solvent (circles and squares) results in an overprediction of the tank-treading frequencies, because the membrane assumes no viscous dissipation. Addition of the membrane viscosity (triangles) reduces the values of the tank-treading frequencies and provides a good agreement with experiments for the membrane viscosity  $\eta_m = 22 \times 10^{-3} Pa \cdot s$ . Note that for all cases a finite intermittent region is observed and it becomes wider for a non-zero membrane viscosity. This result is consistent with the experiments, but it disagrees with the theoretical predictions. Similar results for the intermittent region were reported in simulations of viscoelastic vesicles (42). Moreover, an increase in the internal fluid or membrane viscosities results in a shift of the tumbling-to-tank-treading transition to higher shear rates. Figure 10 (right) shows the average RBC tank-treading angle and the swinging amplitude. The values are consistent with experimental data (1) and appear to be not very sensitive to the membrane viscosity. Note that the swinging frequency is equal to twice the tank-treading frequency.

In conclusion, the RBC model accurately captures membrane dynamics in shear flow, while the theoretical models can predict RBC dynamics *at most* qualitatively. The theoretical models assume ellipsoidal RBC shape and a fixed (ellipsoidal) RBC tank-treading path. Our simulations showed that a RBC is subject to deformations along the tank-treading axis. In addition, modeled RBCs show substantial shape deformations (buckling) in a wide range around the tumbling-to-tank-treading transition. A degree of these deformations depends on the Föppl-von Kármán number  $\kappa$  defined as  $YR_0^2/k_c$ , where  $R_0 = \sqrt{A_0^{tot}/(4\pi)}$ . As an example, if the RBC bending rigidity is increased by a factor of five, the aforementioned shape deformations

become considerably smaller, while if the RBC bending rigidity is increased by a factor of ten, the shape deformations practically subside. The theoretical models do not take the bending rigidity into consideration, while experimental data are not conclusive on this issue. This again raises the question about the magnitude of bending rigidity of healthy RBCs since our simulations (TTC and RBC dynamics in shear flow) indicate that the RBC bending rigidity may be several times higher than the widely used value of  $k_c = 2.4 \times 10^{-19} J$ .

## 4 Validation

In the previous section we demonstrated how we can use experimental data from single-cell measurements to extract the input parameters for the models, but also, to partially validate the simulated biophysical behavior of single RBCs. In this section, we extend this validation further by comparing simulation results based on the MS-RBC model as well as on the LD-RBC model with different experiments. First, we consider data from microfluidic experiments in channels with very small cross-sections, i.e., comparable to the smallest capillaries. We also compare with experimental results from the dynamic response of RBCs going through properly microfabricated geometric constrictions. Subsequently, we present simulation results for whole blood in terms of the flow resistance in tubes and compare against well known experimental results. Finally, we demonstrate how these multiscale simulations can be used as a “virtual rheometer” to obtain the human blood viscosity over a wide range of shear rate values. This includes the low shear rate regime, where the formation of rouleaux is shown to determine the strong non-Newtonian behavior of blood.

### 4.1 Single RBC: Comparison with Microfluidic Experiments

Microfabrication techniques allow manufacturing of channels with dimensions comparable to the smallest blood vessels. In recent years, microfluidic experiments have become popular in measuring properties of RBCs and other cells. Even though, at present time, these experiments typically do not include biochemistry, they can provide quantitative information about the motion of a single RBC through the channels at controlled conditions. This information can be used to validate computational models. The two examples of RBC model validation using microfluidic devices described in this section are taken from refs.(73) and (4), where detailed description of experiments and simulations can be found.

The first set of experiments was performed in the S. Suresh lab at MIT. The channel structures used in these experiments are illustrated in figure 11(a). At their narrowest point, these sharply converging/diverging channels are  $30 \mu m$  long,  $2.7 \mu m$  high and have widths ranging from 3 to  $6 \mu m$ . The experiments were carried out at

temperature 37°C and 41°C. High-speed imaging was used to measure and quantify the temperature-dependent flow characteristics and shape transitions of RBCs as they traversed microfluidic channels of varying size.

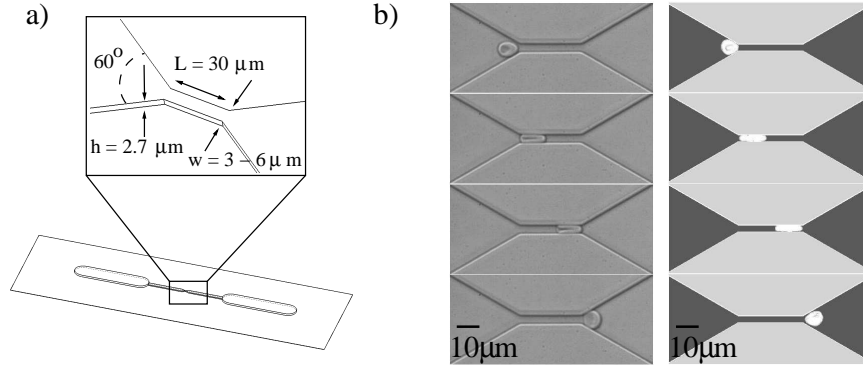


**Fig. 11** (a) Schematic view of microfluidic channels used in experiments. (b) Shape characteristics of RBC traversal across microfluidic channels: Experimental (left) and simulated (right) images of erythrocyte traversal across 4  $\mu\text{m}$  wide, 30  $\mu\text{m}$  long, 2.7  $\mu\text{m}$  high channel at room temperature and an applied pressure difference of 0.085 kPa. (From (4)).

The fluid domain in DPD simulations corresponds to the middle part of the microfluidic device. The width of the flow domain is 60  $\mu\text{m}$ , the length is 200  $\mu\text{m}$ , and the height is 2.7  $\mu\text{m}$ . The central part of the simulation domain is the same as in the experiment. Specifically, the flow is constricted to rectangular cross-section of 4, 5 or 6  $\mu\text{m}$  in width and 2.7  $\mu\text{m}$  in height. The walls are modeled by freezing DPD particles in combination with bounce-back reflection, similar to those in (66). Periodic inlet/outlet boundary conditions are employed, and the flow is sustained by applying an external body force. The RBC model consists of 500 points. Bounce-back reflection is employed at the membrane surface. The internal RBC fluid is 9, 8.5 and 7.6 times more viscous than the external fluid in simulations corresponding to temperature of 22°C, 37°C and 41°C, respectively (68). The effect of temperature in the experiment on the viscosity of the suspending medium is modeled by changing the viscosity of the DPD fluid surrounding the RBC. Specifically, the viscosity of the external fluid at 37°C and 41°C is decreased by 22 % and 28 % compared to the viscosity at 22°C, while the membrane viscosity is decreased by 50 % and 63.5 %, respectively, to match the experimentally measured RBC relaxation times at these temperatures.

Figure 11(b) presents a qualitative comparison of experiment with the DPD model for RBC traversal across a 4  $\mu\text{m}$  wide channel. Here, the cell undergoes a severe shape transition from its normal biconcave shape to an ellipsoidal shape with a longitudinal axis up to 200% of the average undeformed diameter. Figure 12(a) illustrates how the longitudinal axis of the cell, measured at the center of the channel, changes with different channel widths. Experimental and simulated longitudinal

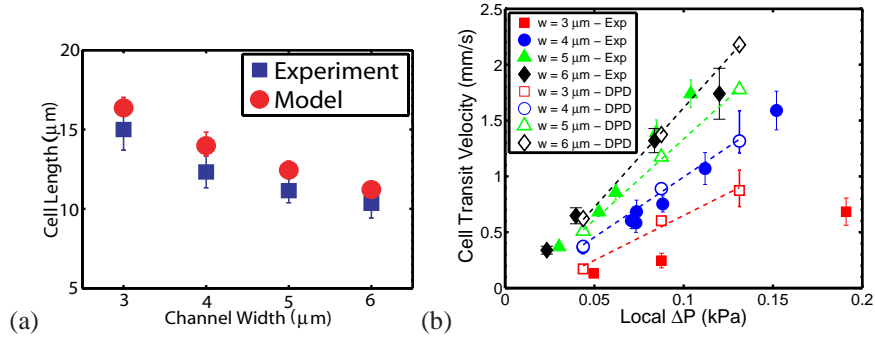


**Fig. 12** Quantitative flow behavior of RBC traversal of microfluidic channels. (a) Measured and simulated cell lengths at the center of the microfluidic channel for varying channel widths. (b) Comparison of DPD simulation results (open markers) with experimentally measured mean velocities (filled markers) of RBC traversal as a function of measured local pressure differences for 3, 4, 5 and 6  $\mu\text{m}$  channel widths (height = 2.7  $\mu\text{m}$ , length = 30  $\mu\text{m}$ ). Error bars on experimental data points represent an average  $\pm$  one standard deviation of a minimum of 18 cells. Error bars on modeling data points indicate minimum and maximum variations resulting from a case study exploring the sensitivity of the RBC traversal to channel geometry and cell volume. (From (73)).

RBC axes typically differ no more than 10-15%. Figure 12(b) presents pressure–velocity relationships for RBC flow across channels of different cross-sectional dimensions. Average cell velocity measurements were taken between the point just prior to the channel entrance (the first frame in Figure 11(b)) and the point at which the cell exits the channel (the final frame in Figure 11(b)). The DPD model adequately captures the scaling of flow velocity with average pressure difference for 4–6  $\mu\text{m}$  wide channels. The significant overlap in the experimental data for 5–6  $\mu\text{m}$  wide channels can be attributed largely to variations in cell size and small variations in channel geometry introduced during their microfabrication. For the smallest channel width of 3  $\mu\text{m}$ , the experimentally measured velocities are as much as half those predicted by the model. This may be attributed to several factors, including non-specific adhesive interactions between the cell membrane and the channel wall due to increased contact. Furthermore, this 3  $\mu\text{m} \times 2.7 \mu\text{m}$  (8.1  $\mu\text{m}^2$ ) cross-section approaches the theoretical 2.8  $\mu\text{m}$  diameter (6.16  $\mu\text{m}^2$ ) limit for RBC transit of axisymmetric pores (5). Therefore, very small variations in channel height (due, for example, to channel swelling/shrinking due to small variations in temperature and humidity) can have significant effects.

For the effect of temperature on the flow dynamics of the RBC we refer the reader to (73) where the ratio of the local pressure gradient and average cell velocity ( $\Delta P/V$ ) as a function of temperature is examined. The main finding is that there exists a threshold cross-section below which the RBC viscous components begin to play a significant role in its dynamic flow behavior; this effect is less profound at higher temperatures. Since the energy dissipation in the membrane is typically higher than in the internal fluid, one might expect the influence of membrane vis-

cosity on the flow behavior of the RBC across such small cross-sections to be large compared to the internal fluid viscosity (19).

The second set of experiments was performed in the J. Han Lab at MIT. The microfluidic device consists of two channels,  $4.2 \mu\text{m}$  in height. Rows of 3 by  $10 \mu\text{m}$  triangular obstacles are placed into the channels as shown in Figure 13(a). The distance between the obstacles is  $3 \mu\text{m}$ , while the distance between rows of obstacles is  $10 \mu\text{m}$ . The only difference between the two channels in the device is the orientation of the obstacles; one channel is the other flipped by  $180^\circ$ .

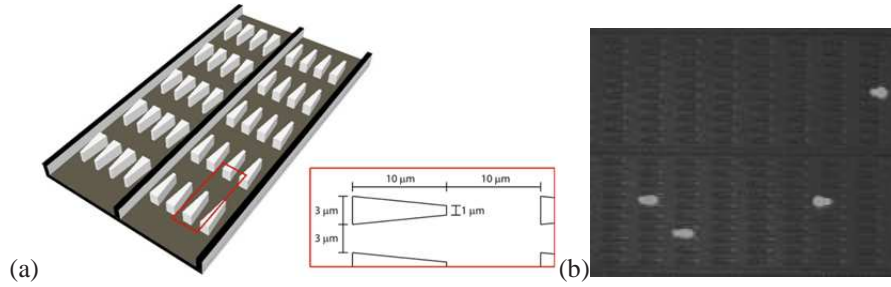


**Fig. 13** (a) Two parallel channels, one with opening geometries that are the reverse of the other, are connected to common inlet and outlet reservoirs. The height of the device is  $4.2 \mu\text{m}$ , the distance between the pillars is  $3 \mu\text{m}$ , and the distance between rows of pillars is  $10 \mu\text{m}$ . (b) Snapshot from video of labeled cells moving through the device. Liquid flow is from right to left. (From (4)).

For low-Reynolds number flows, the resistance and average fluid velocities in the absence of cells must be the same for both channels. When the RBC concentration is low, the cells move with different average velocities in the two channels. This indicates that for openings of the same minimal cross-section area, the geometry (rate) of constriction affects the amount of force required for cell traversal. Also, the channels appear to be sensitive to some specific properties of RBCs, therefore the device can be used to estimate these properties for a given cell from its velocity at known applied pressure gradient.

In simulations, the solid walls are assembled from randomly distributed DPD particles whose positions are fixed. In addition, bounce-back reflections are used to achieve no-slip conditions and prevent fluid particles from penetrating the walls (66). A portion of the microfluidic device with dimensions 200 by 120 by 4.2 microns containing 5 rows of pillars (10 pillars in each row) is modeled. The fluid region is bounded by four walls while periodic boundary conditions are used in the flow direction. Here, the RBC is simulated using 5,000 DPD particles to obtain accurate results unlike most of the other simulations, including the previous example, where 500 DPD points per RBC were sufficient. This is due to the fast dynamic changes of the RBC membrane as the RBC travels through the narrow constrictions. Parameters of the healthy cell model are derived from RBC spectrin network properties as described in previous sections. In addition, membrane fluctuation measurements and optical tweezers experiments are used to define simulation parameters. Specifi-

cally, we required that the amplitude of thermal fluctuations of the membrane at rest to be within the range of experimental observations (65). We also required that the characteristic relaxation time of the RBC model in simulations be equal to the experimentally measured value of 0.18 seconds. The RBC model is immersed into the DPD fluid. The membrane particles interact with internal and external fluid particles through the DPD forces. By changing the direction of the body force, the motion of the cell through channels with converging and diverging pores is simulated using the same channel geometry.

The DPD model is able to capture the effect of obstacle orientation quite accurately. Quantitative comparison of simulation results with experimental data for healthy cell velocity as a function of applied pressure gradient is shown in figure 14.

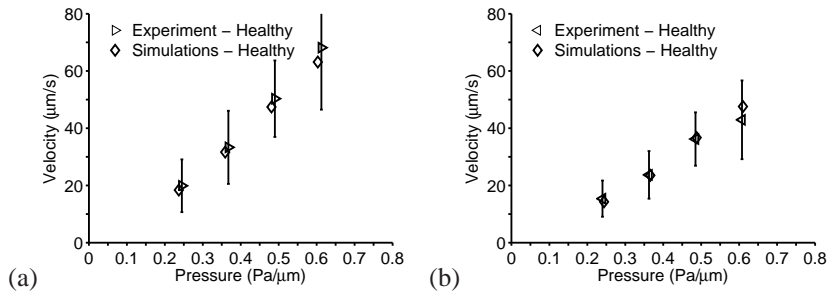


**Fig. 14** Average velocity of healthy RBCs as a function of pressure gradient and comparison of simulation and experimental results. Results for converging (a) and diverging geometries (b). (From (4)).

In order to evaluate contributions of individual mechanical properties of the cell to overall dynamic behavior, we run additional simulations. The DPD model provides a unique opportunity to perform this analysis, since experimental evaluation of these contributions is laborious or impossible. Larger cells are found to travel with lower velocities; however, the velocity variation due to cell size is not significant. Additional simulations were performed in which the membrane shear modulus and membrane viscosity were varied independently of each other. The results showed that the RBC velocity in the device is sensitive to shear modulus, while (in contrast to the device described above) variation of membrane viscosity did not affect the RBC traversal significantly. This finding may seem to be counter intuitive; when the membrane viscosity is increased one would expect higher energy dissipation and therefore lower RBC velocity. Indeed, increased membrane viscosity increases the time it takes for a RBC to traverse an individual opening between pair of obstacles. However, it also slows down the recovery of RBC shape when the cell is traveling between rows of obstacles, making it easier to enter the next opening. As a result, the particular design of this device lessens the dependence of the cell velocity on membrane viscosity.

## 4.2 Whole Healthy Blood

Next, we present simulation results for whole blood modeled as a suspension of healthy RBCs using the two RBC models without changing the parameters that we have established from single-cell measurements. We first consider flow in a tube in order to assess flow resistance in microvessels, and subsequently, we focus on Couette flow in order to compare the predicted blood viscosity from rheometric measurements.

### 4.2.1 Flow Resistance

Here, we simulate blood flow in tubes of diameters ranging from  $10\ \mu\text{m}$  to  $40\ \mu\text{m}$ . In case of the MS-RBC model, it is important to model carefully the excluded volume (EV) interactions among cells, which are often implemented through a repulsive force between membrane vertices of different cells. A certain range (force cutoff radius) of the repulsive interactions may impose a non-zero minimum allowed distance between neighboring RBC membranes, which will be called “screening distance” between membranes. The choice of a smaller cutoff radius may result in overlapping of cells, while a larger one would increase the screening distance between cells, which may be unphysical and may strongly affect the results at high volume fractions of RBCs. A better approach is to enforce EV interactions among cells by employing reflections of RBC vertices on the membrane surfaces of other cells yielding essentially a zero screening distance between two RBC surfaces. In addition, we employ a *net repulsion* of RBCs from the wall by properly setting the repulsive force coefficient between the wall particles and the cell vertices.

Figure 15 shows plots of the apparent blood viscosity with respect to the plasma viscosity. The apparent viscosity is defined as follows  $\eta_{app} = \frac{\pi\Delta P D^4}{128QL}$ , where  $\Delta P$  is the pressure difference,  $Q$  is the flow rate, and  $L$  is the length of the tube. It increases for higher  $H_t$  values since higher cell crowding yields larger flow resistance. It is more convenient to consider the relative apparent viscosity defined as  $\eta_{rel} = \frac{\eta_{app}}{\eta_s}$ , where  $\eta_s$  is the plasma viscosity. Figure 15(a) shows the simulated  $\eta_{rel}$  values in comparison with the empirical fit to experiments (71) for the tube diameter range  $10 - 40\ \mu\text{m}$  and  $H_t$  values in the range  $0.15 - 0.45$ . Excellent agreement between simulations and experiments is obtained for the proper EV interactions for all cases tested. The pressure gradients employed here are  $2.633 \times 10^5$ ,  $1.316 \times 10^5$ , and  $6.582 \times 10^4\ \text{Pa/m}$  for tubes of diameters  $10$ ,  $20$ , and  $40\ \mu\text{m}$ , respectively. In the case of low hematocrit  $H_t$  (e.g.,  $0.15$ ) the velocity profiles closely follow parabolic curves in the near-wall region. In the central region of the tube a substantial reduction in velocity is found for all volume fractions in comparison with the parabolic profiles indicating a decrease in the flow rate (26). Figure 15(b) shows results from both the MS-RBC and LD-RBC models for a wider range of tube diameters. The agreement is good between the models and the experimental data represented by an empirical fit; however, it is clear that for vessels with diameter below  $15 - 20$

microns the LD-RBC model fails as the membrane rheology becomes important, which the low-dimensional model does not account for.

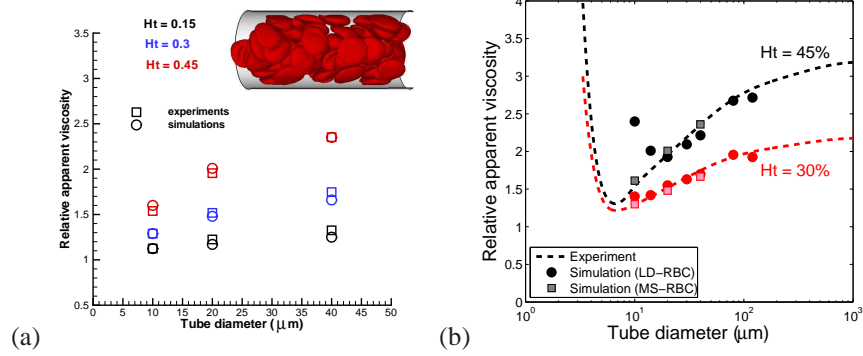


**Fig. 15** Flow resistance in healthy blood: (a) Relative apparent viscosity compared with experimental data (71) for various hematocrit values and tube diameters. The inset plot is a snapshot of RBCs in Poiseuille flow in a tube of a diameter  $D = 20 \mu\text{m}$  at  $H_t = 0.45$ . (b) Comparison of MS-RBC and LD-RBC models; the lines are the empirical correlation by Pries et al. (71). (From (23, 59)).

RBCs in Poiseuille flow migrate to the tube center forming a core in the flow. The inset of Figure 15 shows a sample snapshot of RBCs flowing in a tube of diameter  $D = 20 \mu\text{m}$ . A RBC core formation is established with a thin plasma layer next to the tube walls called the *cell-free* layer (CFL) (26). The thickness of the CFL is directly related to the Fahraeus and the Fahraeus-Lindqvist effects, both of which were accurately captured by the DPD model, see (26). To determine the CFL thickness we computed the outer edge of the RBC core, which is similar to CFL measurements in experiments (43, 49). Figure 16 shows a sample CFL edge from simulations for  $H_t = 0.45$  and  $D = 20 \mu\text{m}$  and local CFL thickness distribution, which is constructed from a set of discrete local measurements of CFL thickness taken every  $0.5 \mu\text{m}$  along the  $x$  (flow) direction. The fluid viscosity of the CFL region is much smaller than that of the tube core populated with RBCs providing an effective lubrication for the core to flow.

#### 4.2.2 Aggregation and Rouleaux Formation

Here, we present simulations in a wide range of shear rate values including the low shear rate regime with and without the aggregation models described in sections 2.3.4 and 2.4.2. The viscosity was derived from simulations of plane Couette flow using the Lees-Edwards periodic boundary conditions in which the shear rate and the density of cells were verified to be spatially uniform. The experimental viscosities of well-prepared erythrocytes without rouleaux and of whole blood were

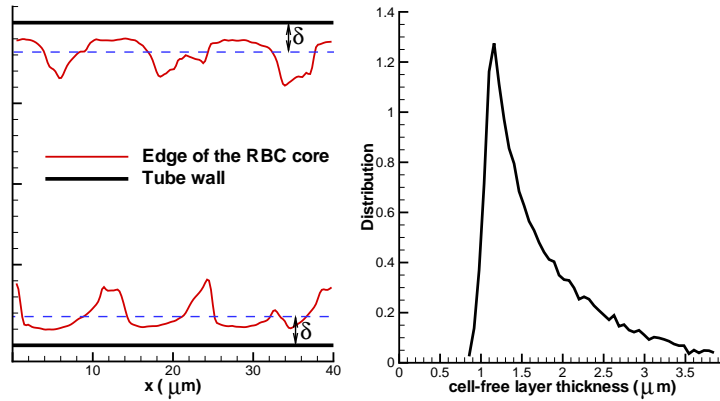


**Fig. 16** An example of a CFL edge (left) and local CFL thickness distribution (right) for  $H_t = 0.45$  and  $D = 20 \mu\text{m}$ . (From (23)).

measured at hematocrit 45% and at temperature  $37^\circ\text{C}$  by (8, 53, 78) using rotational Couette viscometers. At the same conditions for both the MS-RBC and the LD-RBC suspensions the viscosities were computed, with and without rouleaux, as functions of the shear rate over the range  $0.005\text{s}^{-1}$  to  $1000.0\text{s}^{-1}$ . RBC suspension viscosities were normalized by the viscosity values of their suspending media. These data are compared in Figure 17(a) as relative viscosity against shear rate at constant hematocrit. The MS-RBC model viscosity curves lie very close to the viscosities measured in three different laboratories. The model, consisting only of RBCs in suspension, clearly captures the effect of aggregation on the viscosity at low shear rates, and suggests that particles other than RBCs have little effect on the viscosity. The measured values for whole blood are more consistent than those for erythrocyte solutions, which may reflect differences in the preparation of the latter. The LD-RBC model underestimates somewhat the experimental data, but is generally in good agreement over the whole range of shear rates, and again demonstrates the effect of aggregation. This is remarkable in view of the simplicity and economy of that model.

The dependence of whole blood and erythrocyte solution viscosity on hematocrit ( $H_t$ ) is demonstrated in Figure 17(b). The curves are measured viscosities correlated with  $H_t$  at constant shear rate by Chien et al. (8), and the points are calculated with the LD-RBC model. This clearly shows how the latter captures the  $H_t$  dependence of viscosity, and that the model again demonstrates aggregation to be crucial for a quantitative account of the difference between the viscosity of whole blood and that of washed erythrocyte suspensions.

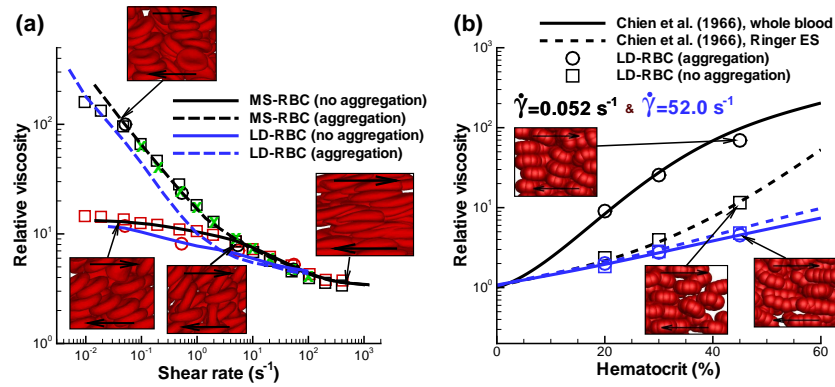


**Fig. 17** Validation of simulation results for whole blood and Ringer erythrocyte solutions (ESs). (a) Plot of non-Newtonian viscosity relative to solvent viscosity as a function of shear rate at  $H_t = 45\%$  and  $37^\circ\text{C}$ : simulated curves of this work, as indicated, and experimental points: Whole blood: green crosses - Merrill et al. (53); black circles - Chien et al. (8), black squares - Skalak et al. (78). Ringer ES: red circles - Chien et al. (8); red squares - Skalak et al. (78). (b) Plot of relative viscosity as a function of hematocrit ( $H_t$ ) at shear rates  $0.052$  (black) and  $52.0$  ( $\text{s}^{-1}$ ): simulated (LD-RBC points), and Chien et al. (8) experimental fits for whole blood (solid lines) and Ringer ES (dashed lines). (From (59)).

## 5 Application to Malaria Modeling

*Plasmodium falciparum* (Pf) causes one of the most serious forms of malaria resulting in several million deaths per year. Pf-parasitized cells (Pf-RBCs) experience progressing changes in their mechanical and rheological properties as well as in their morphology (9, 77) during intra-erythrocytic parasite development, which includes three stages from the earliest to the latest: ring  $\rightarrow$  trophozoite  $\rightarrow$  schizont. Progression through these stages leads to considerable stiffening of Pf-RBCs as found in optical tweezers stretching experiments (82) and in diffraction phase microscopy by monitoring the membrane fluctuations (65). Pf development also results in vacuoles formed inside of RBCs possibly changing the cell volume. Thus, Pf-RBCs at the final stage (schizont) often show a “near spherical” shape, while in the preceding stages maintain their biconcavity. These changes greatly affect the rheological properties and the dynamics of Pf-RBCs, and may lead to obstruction of small capillaries (77) impairing the ability of RBCs to circulate. *In vitro* experiments (2) to investigate the enhanced cytoadherence of Pf-RBCs in flow chambers revealed that their adhesive dynamics can be very different than the well-established adhesive dynamics of leukocytes. For example, the adhesive dynamics of Pf-RBCs on purified ICAM-1 is characterized by stable and persistent flipping (rolling) behavior for a wide range of wall shear stresses (2) but also by intermittent pause and sudden flipping due to the parasite mass inertia.

In this section, we apply the computational framework we developed for healthy RBCs to Pf-RBCs. In particular, we first consider single RBCs for validation pur-

poses and subsequently we simulate whole infected blood as suspension of a mixture of healthy and Pf-RBCs. We examine the mechanical, dynamic and rheologic responses as well as the adhesive dynamics of infected RBCs.

## 5.1 Single Cell

We include in this section comparison with optical tweezers experiments and with microfluidics to assess the fidelity of the RBC models to reproduce the mechanics and dynamics of Pf-RBCs.

### 5.1.1 Mechanics

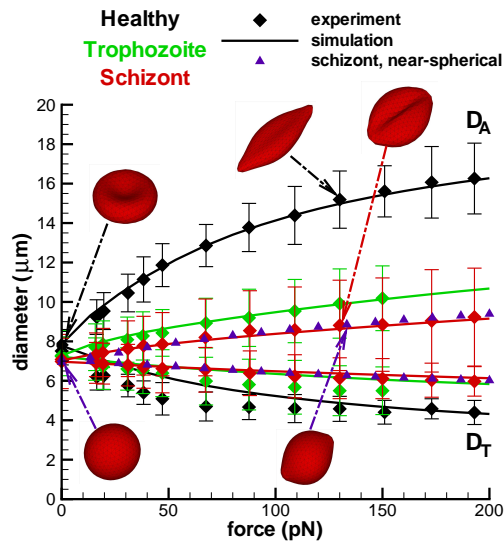


**Fig. 18** Stretching response of Pf-RBCs using the MS-RBC for different stages compared with the experiments (82).  $D_A$  and  $D_T$  refer to the axial and transverse diameters. (From (23)).

In malaria disease, progression through the parasite development stages leads to a considerable stiffening of Pf-RBCs compared to healthy ones (65, 82). Furthermore, in the schizont stage the RBC shape becomes near-spherical whereas in the preceding stages RBCs maintain their biconcavity. Figure 18 shows simulation results for Pf-RBCs at different stages of parasite development. The simulation results were obtained with the MS-RBC model using 500 points. Table 1 presents the shear moduli of healthy and Pf-RBCs at different stages; these values are consistent with the ex-

periments of (65, 82). The bending rigidity for all cases is set to  $2.4 \times 10^{-19} J$ , which

Healthy	Ring	Trophozoite	Schizont
6.3	14.5	29	60 & 40*

**Table 1** Shear moduli of healthy and Pf-RBCs in  $\mu N/m$  at  $T = 23^\circ C$ . The “\*” denotes a “near-spherical” RBC at the schizont stage.

is the value of bending rigidity for healthy RBCs, as the membrane bending stiffness for different stages is not known. The curve for the schizont stage marked as “near-spherical” corresponds to stretching an ellipsoidal shape with axes  $a_x = a_y = 1.2a_z$ . Here, the membrane shear modulus of  $40 \mu N/m$  matches the stress-strain response with the experiment, i.e., it is smaller than that for the biconcave-shape simulation. For the near-spherical cell the membrane is subject to stronger local stretching for the same uniaxial deformation compared to the biconcave shape. For the deflated biconcave shape, the inner fluid volume can be deformed in response to stretching, while in the near-spherical shape the fluid volume applies additional resistance onto the stretched membrane. Hence, the cell geometry plays an important role, and it has to be closely modeled for accurate extraction of parameters from the optical tweezers experiments.

### 5.1.2 Microfluidics

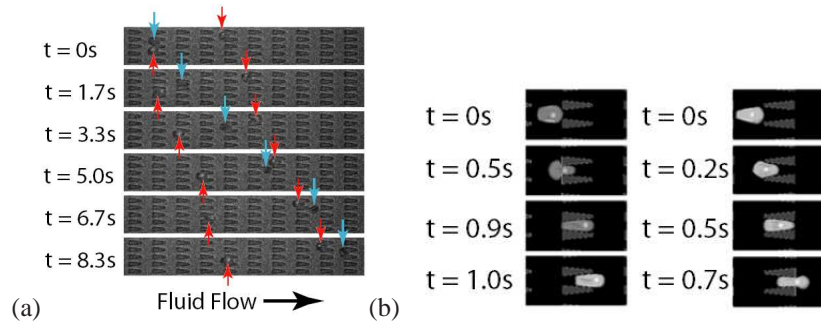


**Fig. 19** (a) Experimental images of ring-stage *P. falciparum*-infected (red arrows) and uninfected (blue arrows) RBCs in the channels at a pressure gradient of  $0.24 Pa/\mu m$ . The small fluorescent dot inside the infected cell is the GFP-transfected parasite. At  $8.3 s$ , it is clear that the uninfected cell moved about twice as far as each infected cell. (b) DPD simulation images of *P. falciparum*-infected RBCs traveling in channels of converging (left) and diverging (right) opening geometry at  $0.48 Pa/\mu m$ . (From (4)).

The microfluidic device with triangular obstacles described in section 4.1 is used also here to perform experiments for the late ring-stage *P.falciparum*-infected RBCs

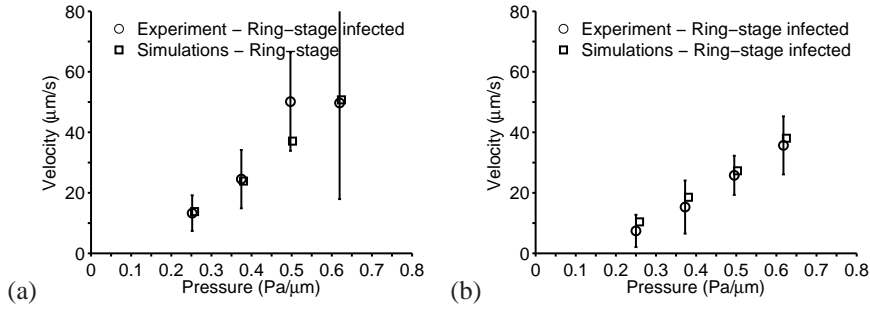


**Fig. 20** Average velocity of ring-stage malaria infected RBCs as a function of pressure gradient and comparison of simulation and experimental results. Results for converging (a) and diverging (b) geometries. (From (4)).

that are infected with a gene encoding green fluorescent protein (GFP). For both the converging and diverging geometries infected RBCs exhibit lower average velocities than healthy RBCs (see figure 19(a)). In the DPD simulations, the infected cells are modeled with increased shear modulus and membrane viscosity values obtained from optical tweezers as explained in the previous section. We model the parasite as a rigid sphere of two microns in diameter (16) placed inside the cell (see figure 1(b)). Snapshots from simulations showing passage of an infected RBC through channels with converging and diverging pore geometries are shown in figure 19(b). The DPD model is able to capture the effect of changes of RBC properties arising from parasitization quite accurately. A quantitative comparison of the simulation results with experimental data for the average velocity of Pf-RBCs as a function of applied pressure gradient is shown in figure 20.

### 5.1.3 Pf-RBC Adhesive Dynamics

Here, we present typical results for the adhesive dynamics of Pf-RBCs in shear flow for various values of the wall shear stress (WSS). The models employed are described in section 2.3.5 with some modifications in order for the simulated RBC dynamics to be comparable with that found in experiments (2) using purified ICAM-1 as a wall coating. Figure 21 shows several successive snapshots of a cell rolling on the wall for the schizont stage of a Pf-RBC. The dynamics of the Pf-RBC is characterized by a “flipping” behavior initiated first by the cell peeling off the wall due to the force of the hydrodynamic flow after flat RBC adhesion (the first snapshot in figure 21). After the majority of the initial cell contact area with the wall is peeled off, a RBC flips over on its other side which is facilitated by the remaining small contact area with the wall. During these steps Pf-RBCs undergo strong membrane deformations as illustrated in figure 21. A similar behavior was found in experiments (2) of Pf-RBCs which showed flipping (rolling) along a wall coated

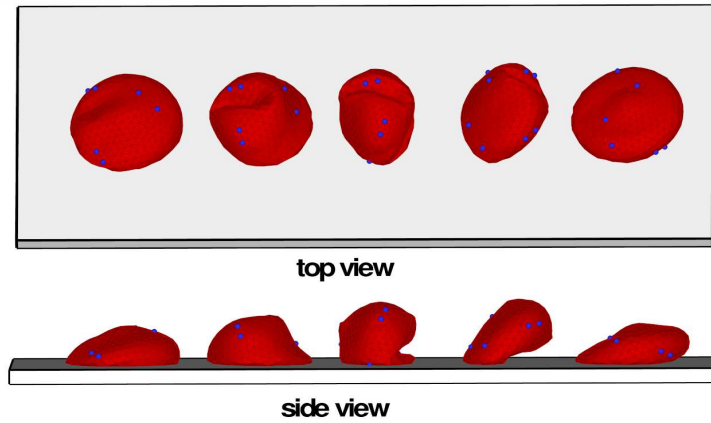


**Fig. 21** Top and side views of successive snapshots of a single flipping of an infected RBC at the schizont stage. Coordinates along the wall for different snapshots are shifted in order to separate them for visual clarity. Blue particles are added as tracers during post-processing to illustrate the membrane dynamics. (From (23)).

with purified ICAM-1. In agreement with the simulations, RBCs in experiments also showed strong membrane deformations characterized by local membrane buckling.

Figure 22 presents the corresponding displacement along the  $x$  coordinate (a) and instantaneous RBC velocity (b). An infected RBC rolls in a relatively stable motion

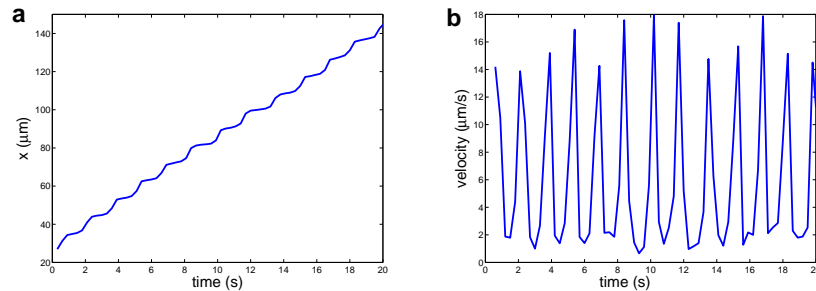


**Fig. 22** Pf-RBC displacement (a) and velocity (b) along the wall for the schizont stage. (From (23)).

which resembles a staircase. The segments of smaller displacements correspond to the stage of a flat RBC adhesion followed by its slow peeling off the wall (see figure 21), while the fragments of larger displacements represent the stage of RBC fast flipping described above. The RBC velocity is in agreement with its displacement showing high peaks or fast cell motion during the time segments with larger displacements. The average cell velocity is approximately  $5.8 \mu\text{m/s}$ . Figure 23 shows RBC displacement along the  $z$  cross-flow coordinate (a) and instantaneous contact

area (b). The displacement across the wall shows a jerky motion of an infected RBC

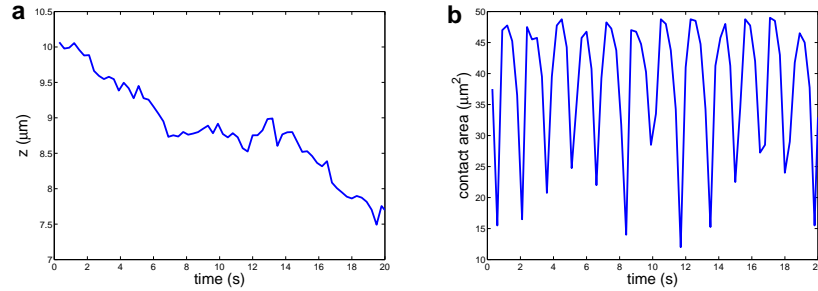


**Fig. 23** RBC displacement across the wall (a) and the cell contact area (b) for the schizont stage. (From (23)).

within several microns. This is due to the discrete number of bonds and their random rupture or dissociation. Thus, if there is a non-uniform distribution of bonds over the contact area at some instance of time, a Pf-RBC may be pulled to one side. In addition, the hydrodynamic force on the RBC may be non-zero in  $z$  direction, since the cell is not symmetric due to the local deformations shown in figure 21. The RBC contact area in figure 23(b) is correlated with its displacement and velocity in figure 22. Minima in the contact area coincide with maxima in the RBC velocity corresponding to the stage of fast cell flipping from its one side to the other. The cell contact area remains within the range of  $10 - 50 \mu\text{m}^2$ , while the average value is equal to  $38.6 \mu\text{m}^2$ .

To investigate the dependence of RBC adhesive dynamics on WSS, the velocity of the upper plate is changed. Note that the shear rate is altered at the same time. However, the WSS appears to be a key parameter which governs RBC adhesive dynamics, since adhered RBCs are driven by fluid stresses and roll along the wall with a much smaller velocity than that of the shear flow.

Several initial simulations with a varying WSS and other fixed parameters revealed that a Pf-RBC may exhibit firm adhesion at a WSS lower than  $0.317 \text{ Pa}$  for the case described above and can completely detach from the wall at higher WSS. At low WSS, adhesion forces are strong enough to counteract the stress exerted on the cell by the flow resulting in its firm sticking to the lower wall. On the contrary, at high WSS existing bonds do not provide sufficiently strong adhesive interactions which yields RBC detachment from the wall. RBC visualizations showed that its detachment at high WSS occurs during the relatively fast motion of RBC flipping, since the contact area at that step corresponds to its minimum. However, in experiments (2) Pf-RBCs which moved on a surface coated with the purified ICAM-1 showed persistent and stable rolling over long observation times and for a wide range of WSS between  $0.2 \text{ Pa}$  and  $2 \text{ Pa}$ . This suggests that there must be a mechanism which stabilizes rolling of infected RBCs at high WSS. This fact is not sur-

prising since, for example, leukocyte adhesion can be actively regulated depending on flow conditions and biochemical constituents present (28, 80).

To stabilize RBC binding at high WSS we introduce adaptivity of the bond spring constant ( $k_s$ ) see equation (29). As the first approximation we assume a linear dependence of  $k_s$  on the WSS, such that  $k_s$  is increased or decreased proportionally to an increase or decrease in the WSS. Figure 24 presents the average rolling velocity of a Pf-RBC in comparison with experiments of cell rolling on a surface coated with purified ICAM-1 (2). The simulated average velocities for the “linear” case show a

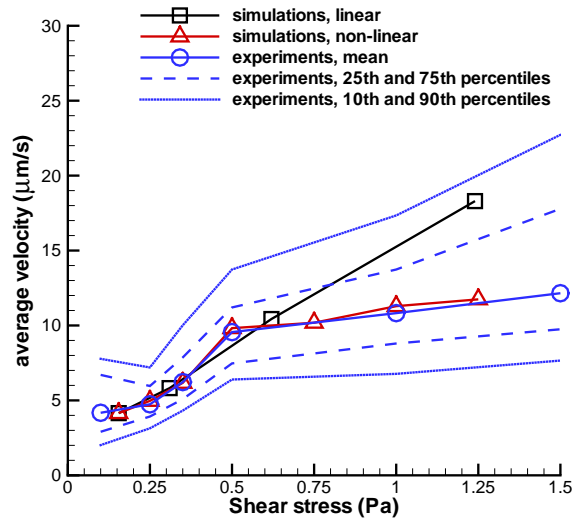


**Fig. 24** Average rolling velocity of infected RBCs depending on the WSS in comparison with the experiments of cell rolling on purified ICAM-1 (2). Experimental data include mean values and curves that correspond to the 10th, 25th, 75th, and 90th percentiles. (From (23)).

near-linear dependence on the WSS and are in good agreement with experiments up to some WSS value; the simulated value remains between the 10th and the 90th percentiles found in experiments. However, the observed discrepancy at the highest simulated WSS suggests that a further strengthening of cell-wall bond interactions may be required. The dependence of the RBC rolling velocity on WSS found in experiments is clearly non-linear. Therefore, the assumption of linear dependence of  $k_s$  on the WSS is likely to be an oversimplification. The simulation results marked “non-linear” in figure 24 adopt a non-linear dependence of  $k_s$  on the WSS, and yield excellent agreement with experiments.

In addition, there may be a change in bond association and dissociation kinetics with WSS which would be able to aid in rolling stabilization of infected RBCs at high shear rates. The DPD simulations suggest that the adhesive dynamics of Pf-RBCs is not very sensitive to a moderate change (below 30% – 40%) in  $k_{on}^0$  and  $k_{off}^0$ ;

however, cell dynamics may be strongly affected if these parameters are changed considerably. Moreover, experimental data show a much larger scatter in the average RBC velocity for different cells observed than that in simulations (not shown). This is likely to be related to non-uniform distributions of receptors on the RBC membrane and ligands on the wall. In the simulations, distributions of both receptors and ligands are fixed and are nearly homogeneous with approximately the same area occupied by each receptor or each ligand. A scatter in behavior among distinct RBCs in the simulations is solely related to the stochastic nature of the adhesive model. However, in experiments irregular distributions of receptors and ligands are likely to significantly contribute to a scatter in RBC adhesive dynamics.

## 5.2 Whole Infected Blood

Finally, we simulate blood flow in malaria as a suspension of healthy and Pf-RBCs at the trophozoite stage and hematocrit  $H_t = 0.45$ . Several parasitemia levels (percentage of Pf-RBCs with respect to the total number of cells in a unit volume) from 5% to 100% are considered in vessels with diameters 10 and 20  $\mu\text{m}$ . The inset of figure 25 shows a snapshot of RBCs flowing in a tube of diameter 20  $\mu\text{m}$  at a parasitemia level of 25%. The main result in figure 25(a) is given by the plot of

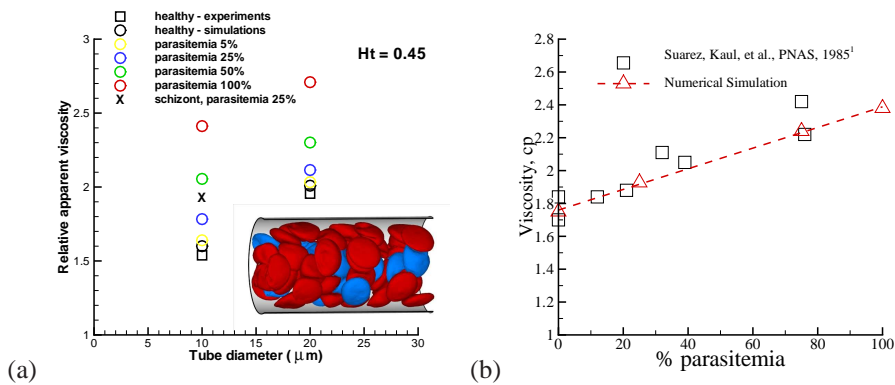


**Fig. 25** Flow resistance in malaria: (a) Healthy (red) and Pf-RBCs (blue) in Poiseuille flow in a tube of diameter  $D = 20 \mu\text{m}$ .  $H_t = 0.45$ , parasitemia level 25%. Plotted is the relative apparent viscosity of blood in malaria for various parasitemia levels and tube diameters. Symbol “x” corresponds to the schizont stage with a near-spherical shape. Experimental data from the empirical fit by Pries et al. (71). (From (23)). (b) Bulk viscosity versus parasitemia level for 30% hematocrit using a Couette device setup at shear rate  $230 \text{ s}^{-1}$ . The square symbols are measurements from (74) and the triangles are simulations of Huan Lei (Brown University).

the relative apparent viscosity in malaria – a measure of flow resistance as in section 4.2 – obtained at different parasitemia levels. The effect of parasitemia level

appears to be more prominent for small diameters and high  $H_t$  values. Thus, at  $H_t = 0.45$  blood flow resistance in malaria may increase up to 50% in vessels of diameters around  $10 \mu m$  and up to 43% for vessel diameters around  $20 \mu m$ . These increases do not include any contributions from the interaction of Pf-RBCs with the glycocalyx (68, 88); such important interactions are complex as they may include cytoadhesion. In figure 25(b) we also present the bulk viscosity of infected blood (schizont stage) simulated in a Couette type device at shear rate  $\gamma = 230 s^{-1}$ . The DPD simulations compare favorably with the experimental data obtained with a corresponding rheometer in (74). These validated predictions were obtained without an explicit adhesion model between Pf-RBCs. It seems that such cell-cell interactions are not important at this high shear rate value.

## 6 Summary

In this chapter we have presented a comprehensive simulation methodology based on dissipative particle dynamics (DPD), which is effective in predicting the blood flow behavior (mechanics, dynamics and rheology) in health and disease. We emphasized, in particular, how single-RBC experiments – using optical tweezers and novel microfluidic devices – can provide data from which we can extract the macroscopic parameters of the model, which can then be related to the microscopic parameters required by the two RBC models we presented. In addition, these single-RBC data can serve as a validation test bed over a wide range of operating conditions. The success of the DPD models is then to predict *whole blood* behavior in health or disease without any further “tuning” of the models’ parameters. We demonstrated that this is indeed the case for healthy and malaria-infected whole blood in two different set ups, i.e., blood flow in a tube as well as in Couette flow. In particular, we presented accurate predictions of the bulk viscosity both for healthy blood as well as for infected blood with parasitemia levels up to 100%.

The two RBC models we presented can be used in a complementary fashion in simulations of hematologic disorders. The multiscale model (MS-RBC) can resolve structures down to protein level on the lipid bilayer or the spectrin level of the cytoskeleton and can be used efficiently for whole blood simulations (up to 45% hematocrit) for capillaries and arterioles of approximately up to 100 microns in diameter. On the other hand, the more economical low-dimensional model (LD-RBC) does not account for the membrane explicitly and it is only accurate, as we demonstrated in section 4, for arterioles, i.e. vessels with diameter above 15 – 20 microns. That too, however, can become computationally expensive for high hematocrit values and for large arteries. To this end, a continuum model can be employed above a certain vessel size with the Newtonian constitutive law valid for blood for that size of arterial vessels. This multiscale approach, which is appropriate for the entire human arterial tree, is demonstrated diagrammatically in the sketch of figure 26.

Next, we comment further on the RBC model parameters used as input from experimental data, which can be roughly divided into three groups: (1) RBC prop-

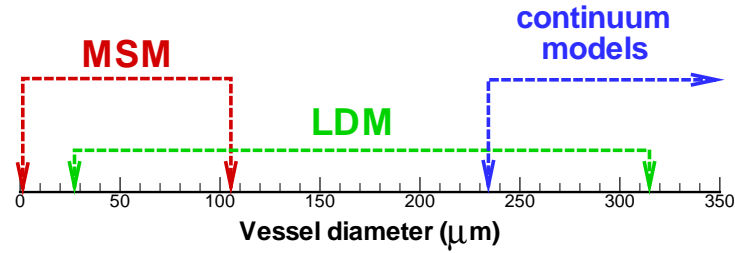


**Fig. 26** Applicability of different models with respect to a characteristic vessel size (diameter).

erties, e.g., geometry, shear and bending moduli, membrane viscosity, parasite in malaria, polymerized hemoglobin in sickle cell anemia, etc.; (2) adhesion properties, e.g., receptor and ligand densities, on and off rates, and bond stiffness, and (3) flow properties, e.g., shear rate, fluid viscosity. The flow properties can be effectively reduced to a single parameter, e.g., the wall shear stress (WSS), which is the governing parameter and can influence greatly the adhesive dynamics as we demonstrated in the case of malaria. Often the dominant RBC parameter is the shear modulus not only in the static but also in the dynamic response. For example, the increased shear modulus of Pf-RBCs in comparison with healthy RBCs is the main reason for the flipping motion of Pf-RBCs. Cell geometry could be also very important, for example more spherical Pf-RBCs will likely roll on a surface than flip; shape changes are particularly influential in sickle cell anemia, spherocytosis and elliptocytosis. On the other hand, the RBC bending rigidity seems to play a secondary role in the mechanics or dynamics, and in most cases the membrane viscosity also plays a secondary role, but not for very small capillaries, as we discussed in section 4.1. For diseased RBCs, the adhesion parameters govern the states of adhesion, e.g., firm adhesion, flipping, slipping, detachment. For leukocytes, these different states have been studied thoroughly, e.g. (44) and agree well with the plethora of experimental data. In summary, for fixed flow conditions and cell parameters, the space of adhesion parameters can be divided into sub-spaces with different adhesion states. A similar adhesion state diagram can be constructed for diseased RBCs with adhesive properties, but experimental data are currently lacking.

Finally, we want to clarify that we modeled here whole blood as suspension of RBCs in plasma, hence ignoring the effect of white cells (about 0.7%) and platelets (less than 0.5% ) or the effect of other proteins in the plasma, although we modeled fibrinogen implicitly in section 4 on rouleaux formation. From the numerical modeling standpoint, there is no particular difficulty in also modeling these other cells, which are significant in specific biomedical studies, e.g. in thrombosis, immune response. From the biophysical view point, however, as we demonstrated in sections 4 and 5 their presence is not important for the whole blood rheological properties.

**Acknowledgements** This work was supported by NIH and NSF. Simulations were performed at the NSF supercomputing center NICS, at the BG/P at ANL via an INCITE DOE award, and at the Jülich supercomputing center.

## References

- [1] Abkarian, M., Faivre, M., Viallat, A.: Swinging of red blood cells under shear flow. *Physical Review Letters* **98**, 188,302 (2007)
- [2] Antia, M., Herricks, T., Rathod, P.K.: Microfluidic modeling of cell-cell interactions in malaria pathogenesis. *PLoS Pathogens* **3**(7), 939–945 (2007)
- [3] Beck, W.S. (ed.): *Hematology*, fifth edn. MIT Press (1991)
- [4] Bow, H., Pivkin, I.V., Diez-Silva, M., Goldfless, S.J., Dao, M., Niles, J.C., Suresh, S., Han, J.: A microfabricated deformability-based flow cytometer with application to malaria. *Lab on a Chip*, submitted (2010)
- [5] Canham, P.B., Burton, A.C.: Distribution of size and shape in populations of normal human red cells. *Circulation Research* **22**(3) (1968)
- [6] Chaudhuri, O., Parekh, S., Lam, W., Fletcher, D.: Combined atomic force microscopy and side-view optical imaging for mechanical studies of cells. *Nature Methods* **6** (5), 383–387 (2009)
- [7] Chien, S., Jan, K.M.: Ultrastructural basis of the mechanism of rouleaux formation. *Microvascular Research* **5**, 155–166 (1973)
- [8] Chien, S., Usami, S., Taylor, H.M., Lundberg, J.L., Gregersen, M.I.: Effects of hematocrit and plasma proteins on human blood rheology at low shear rates. *Journal of Applied Physiology* **21**, 817 (1966)
- [9] Cranston, H.A., Boylan, C.W., Carroll, G.L., Sutura, S.P., Williamson, J.R., Gluzman, I.Y., Krogstad, D.J.: *Plasmodium falciparum* maturation abolishes physiologic red cell deformability. *Science* **223**, 400–403 (1984)
- [10] Diez-Silva, M., Dao, M., Han, J., Lim, C.T., Suresh, S.: Shape and biomechanical characteristics of human red blood cells in health and disease. *MRS Bulletin* **35**, 382–388 (2010)
- [11] Discher, D.E., Boal, D.H., Boey, S.K.: Simulations of the erythrocyte cytoskeleton at large deformation. II. Micropipette aspiration. *Biophysical Journal* **75**(3), 1584–1597 (1998)
- [12] Discher, D.E., Mohandas, N., Evans, E.A.: Molecular maps of red cell deformation: hidden elasticity and in situ connectivity. *Science* **266**, 1032–1035 (1994)
- [13] Dupin, M.M., Halliday, I., Care, C.M., Alboul, L., Munn, L.L.: Modeling the flow of dense suspensions of deformable particles in three dimensions. *Physical Review E* **75**(6), 066,707 (2007)
- [14] Dzwinel, W., Boryczko, K., Yuen, D.A.: A discrete-particle model of blood dynamics in capillary vessels. *Journal of Colloid and Interface Science* **258**(1), 163–173 (2003)

- [15] Eggleton, C.D., Popel, A.S.: Large deformation of red blood cell ghosts in a simple shear flow. *Physics of Fluids* **10**(8), 1834 (1998)
- [16] Enderle, T., Ha, T., Ogletree, D.F., Chemla, D.S., Magowan, C., Weiss, S.: Membrane specific mapping and colocalization of malarial and host skeletal proteins in the plasmodium falciparum infected erythrocyte by dual-color near-field scanning optical microscopy. *Proceedings of the National Academy of Sciences of the United States of America* **94**(2), 520–525 (1997)
- [17] Espanol, P.: Fluid particle model. *Physical Review E* **57**(3), 2930 (1998)
- [18] Espanol, P., Warren, P.: Statistical mechanics of dissipative particle dynamics. *Europhysics Letters* **30**(4), 191–196 (1995)
- [19] Evans, E.A., Hochmuth, R.M.: Membrane viscoelasticity. *Biophysical Journal* **16**(1), 1–11 (1976)
- [20] Evans, E.A., Skalak, R.: *Mechanics and thermodynamics of biomembranes*. CRC Press, Inc., Boca Raton, Florida (1980)
- [21] Fan, X., Phan-Thien, N., Chen, S., Wu, X., Ng, T.Y.: Simulating flow of DNA suspension using dissipative particle dynamics. *Physics of Fluids* **18**(6), 063,102 (2006)
- [22] Fan, X.J., Phan-Thien, N., Chen, S., Wu, X.H., Ng, T.Y.: Simulating flow of DNA suspension using dissipative particle dynamics. *Physics of Fluids* **18**(6), 063,102 (2006)
- [23] Fedosov, D.A.: *Multiscale modeling of blood flow and soft matter*. PhD thesis, Brown University, USA (2010)
- [24] Fedosov, D.A., Caswell, B., Karniadakis, G.E.: A multiscale red blood cell model with accurate mechanics, rheology, and dynamics. *Biophysical Journal* **98**(10), 2215–2225 (2010)
- [25] Fedosov, D.A., Caswell, B., Karniadakis, G.E.: Systematic coarse-graining of spectrin-level red blood cell models. *Computer Methods in Applied Mechanics and Engineering* **199**, 1937–1948 (2010)
- [26] Fedosov, D.A., Caswell, B., Popel, A.S., Karniadakis, G.E.: Blood flow and cell-free layer in microvessels. *Microcirculation* **17**, 615–628 (2010)
- [27] Fedosov, D.A., Pivkin, I.V., Karniadakis, G.E.: Velocity limit in DPD simulations of wall-bounded flows. *Journal of Computational Physics* **227**(4), 2540–2559 (2008)
- [28] Finger, E.B., Puri, K.D., Alon, R., Lawrence, M.B., von Andrian, U.H., Springer, T.A.: Adhesion through L-selectin requires a threshold hydrodynamic shear. *Nature (London)* **379**, 266–269 (1996)
- [29] Fischer, T.M.: Shape memory of human red blood cells. *Biophysical Journal* **86**(5), 3304–3313 (2004)
- [30] Fischer, T.M.: Tank-tread frequency of the red cell membrane: Dependence on the viscosity of the suspending medium. *Biophysical Journal* **93**(7), 2553–2561 (2007)
- [31] Fung, Y.C.: *Biomechanics: Mechanical properties of living tissues*, second edn. Springer-Verlag, New York (1993)
- [32] Gov, N.S.: Active elastic network: cytoskeleton of the red blood cell. *Physical Review E* **75**(1), 011,921 (2007)

- [33] Gov, N.S., Safran, S.A.: Red blood cell membrane fluctuations and shape controlled by ATP-induced cytoskeletal defects. *Biophysical Journal* **88**, 1859–1874 (2005)
- [34] Groot, R.D., Warren, P.B.: Dissipative particle dynamics: Bridging the gap between atomistic and mesoscopic simulation. *Journal of Chemical Physics* **107**(11), 4423–4435 (1997)
- [35] Hammer, D.A., Apte, S.M.: Simulation of cell rolling and adhesion on surfaces in shear flow: general results and analysis of selectin-mediated neutrophil adhesion. *Biophysical Journal* **63**, 35–57 (1992)
- [36] Helfrich, W.: Elastic properties of lipid bilayers: theory and possible experiments. *Z. Naturforschung C* **28**, 693–703 (1973)
- [37] Henon, S., Lenormand, G., Richert, A., Gallet, F.: A new determination of the shear modulus of the human erythrocyte membrane using optical tweezers. *Biophysical Journal* **76**, 1145–1151 (1999)
- [38] Higgins, J., Eddington, D., Bhata, S., Mahadevan, L.: Sick cell vasoocclusion and rescue in a microfluidic device. *Proceedings of the National Academy of Sciences USA* **104**(51), 20,496 (2007)
- [39] Ho, M., White, N.J.: Molecular mechanisms of cytoadherence in malaria. *American Journal of Physiology* **276**, C1231–C1242 (1999)
- [40] Hoogerbrugge, P.J., Koelman, J.M.V.A.: Simulating microscopic hydrodynamic phenomena with dissipative particle dynamics. *Europhysics Letters* **19**(3), 155–160 (1992)
- [41] Howard, R.J.: Malarial proteins at the membrane of *Plasmodium falciparum*-infected erythrocytes and their involvement in cytoadherence to endothelial cells. *Progress in Allergy* **41**, 98–147 (1988)
- [42] Kessler, S., Finken, R., Seifert, U.: Swinging and tumbling of elastic capsules in shear flow. *Journal of Fluid Mechanics* **605**, 207–226 (2008)
- [43] Kim, S., Long, L.R., Popel, A.S., Intaglietta, M., Johnson, P.C.: Temporal and spatial variations of cell-free layer width in arterioles. *American Journal of Physiology* **293**, H1526–H1535 (2007)
- [44] Korn, C.B., Schwarz, U.S.: Dynamic states of cells adhering in shear flow: From slipping to rolling. *Physical Review E* **77**(4), 041,904 (2008)
- [45] Lei, H., Caswell, B., Karniadakis, G.: Direct comparison of mesoscopic models from microscopic simulations. *Physical Review. E* **81**, 026,704 (2010)
- [46] Li, J., Dao, M., Lim, C.T., Suresh, S.: Spectrin-level modeling of the cytoskeleton and optical tweezers stretching of the erythrocyte. *Biophysical Journal* **88**, 3707–3719 (2005)
- [47] Li, J., Lykotrafitis, G., Dao, M., Suresh, S.: Cytoskeletal dynamics of human erythrocyte. *Proceedings of the National Academy of Sciences USA* **104**(12), 4937–4942 (2007)
- [48] Liu, Y., Liu, W.K.: Rheology of red blood cell aggregation by computer simulation. *Journal of Computational Physics* **220**, 139–154 (2006)
- [49] Maeda, N., Suzuki, Y., Tanaka, J., Tateishi, N.: Erythrocyte flow and elasticity of microvessels evaluated by marginal cell-free layer and flow resistance. *American Journal of Physiology* **271**(6), H2454–H2461 (1996)

- [50] Magowan, C., Brown, J.T., Liang, J., Heck, J., Coppel, R.L., Mohandas, N., MeyerIlse, W.: Intracellular structures of normal and aberrant plasmodium falciparum malaria parasites imaged by soft x-ray microscopy. *Proceedings of the National Academy of Sciences of the United States of America* **94**(12), 6222–6227 (1997)
- [51] Malevanets, A., Kapral, R.: Mesoscopic model for solvent dynamics. *Journal of Chemical Physics* **110**(17), 8605–8613 (1999)
- [52] Marinkovic, M., Diez-Silva, M., Pantic, I., Fredberg, J.J., Suresh, S., Butler, J.P.: Febrile temperature leads to significant stiffening of Plasmodium falciparum parasitized erythrocytes. *American Journal of Physiology: Cell Physiology* **296**, C59–C64 (2009)
- [53] Merrill, E.W., Gilliland, E.R., Cokelet, G., Shin, H., Britten, A., Wells, R.E.: Rheology of human blood near and at zero flow. *Biophysical Journal* **3**, 199–213 (1963)
- [54] Puig-de Morales-Marinkovic, M., Turner, K.T., Butler, J.P., Fredberg, J.J., Suresh, S.: Viscoelasticity of the human red blood cell. *American Journal of Physiology: Cell Physiology* **293**, 597–605 (2007)
- [55] Nagao, E., Kaneko, O., Dvorak, J.A.: Plasmodium falciparum-infected erythrocytes: qualitative and quantitative analyses of parasite-induced knobs by atomic force microscopy. *Journal of Structural Biology* **130**, 34–44 (2000)
- [56] Neu, B., Meiselman, H.J.: Depletion-mediated red blood cell aggregation in polymer solutions. *Biophysical Journal* **83**, 2482–2490 (2002)
- [57] Noguchi, H., Gompper, G.: Dynamics of fluid vesicles in shear flow: Effect of the membrane viscosity and thermal fluctuations. *Physical Review E* **72**(1), 011,901 (2005)
- [58] Noguchi, H., Gompper, G.: Shape transitions of fluid vesicles and red blood cells in capillary flows. *Proceedings of the National Academy of Sciences USA* **102**(40), 14,159–14,164 (2005)
- [59] Pan, W.: Single particle DPD: Algorithms and applications. PhD Thesis, Brown University (2010)
- [60] Pan, W., Caswell, B., Karniadakis, G.E.: A low-dimensional model for the red blood cell. *Soft Matter* **6**, 4366–4376 (2010)
- [61] Pan, W., Caswell, B., Karniadakis, G.E.: Rheology, microstructure and migration in brownian colloidal suspensions. *Langmuir* **26**(1), 133–142 (2010)
- [62] Pan, W., Fedosov, D.A., Caswell, B., Karniadakis, G.E.: Hydrodynamic interactions for single dissipative-particle-dynamics particles and their clusters and filaments. *Physical Review E* **78**(4), 046,706 (2008)
- [63] Pan, W., Pivkin, I.V., Karniadakis, G.E.: Single-particle hydrodynamics in DPD: A new formulation. *Europhysics Letters* **84**(1), 10,012 (2008)
- [64] Park, Y., Best, C., Auth, T., Gov, N., Safran, G., Popescu, G., Suresh, S., Feld, M.: Metabolic remodeling of the human red blood cell membrane. *Proceedings of the National Academy of Sciences USA* **107**(4), 1289 (2010)
- [65] Park, Y.K., Diez-Silva, M., Popescu, G., Lykotraftis, G., Choi, W., Feld, M.S., Suresh, S.: Refractive index maps and membrane dynamics of human red

- blood cells parasitized by *Plasmodium falciparum*. Proceedings of the National Academy of Sciences USA **105**(37), 13,730–13,735 (2008)
- [66] Pivkin, I.V., Karniadakis, G.E.: A new method to impose no-slip boundary conditions in dissipative particle dynamics. *Journal of Computational Physics* **207**(1), 114–128 (2005)
- [67] Pivkin, I.V., Karniadakis, G.E.: Accurate coarse-grained modeling of red blood cells. *Physical Review Letters* **101**(11), 118,105 (2008)
- [68] Popel, A.S., Johnson, P.C.: Microcirculation and hemorheology. *Annual Review of Fluid Mechanics* **37**, 43–69 (2005)
- [69] Popescu, G., Park, Y.K., Dasari, R.R., Badizadegan, K., Feld, M.S.: Coherence properties of red blood cell membrane motions. *Physical Review E* **76**(3), 031,902 (2007)
- [70] Pozrikidis, C.: Numerical simulation of cell motion in tube flow. *Annals of Biomedical Engineering* **33**(2), 165–178 (2005)
- [71] Pries, A.R., Neuhaus, D., Gaehtgens, P.: Blood viscosity in tube flow: dependence on diameter and hematocrit. *American Journal of Physiology* **263**(6), H1770–H1778 (1992)
- [72] Pryamitsyn, V., Ganesan, V.: A coarse-grained explicit solvent simulation of rheology of colloidal suspensions. *Journal of Chemical Physics* **122**(10), 104,906 (2005)
- [73] Quinn, D.J., Pivkin, I.V., Wong, S.Y., Chiam, K.H., Dao, M., Karniadakis, G.E., Suresh, S.: Combined simulation and experimental study of large deformation of red blood cells in microfluidic systems. *Annals of Biomedical Engineering*, to appear (2010)
- [74] Raventos-Suarez, C., Kaul, D., Nagel, R.: Membrane knobs are required for the microcirculatory obstruction induced by *plasmodium falciparum*-infected erythrocytes. *Proceedings of the National Academy of Sciences USA* **82**, 3829–3833 (1985)
- [75] Rosenbluth, M., Lam, W., Fletcher, D.: Analyzing cell mechanics in hematologic diseases with microfluidic biophysical flow cytometry. *Lab on a Chip* **8**, 1062–1070 (2008)
- [76] Seung, H.S., Nelson, D.R.: Defects in flexible membranes with crystalline order. *Physical Review A* **38**(2), 1005–1018 (1988)
- [77] Shelby, J.P., White, J., Ganesan, K., Rathod, P.K., Chiu, D.T.: A microfluidic model for single-cell capillary obstruction by *Plasmodium falciparum*-infected erythrocytes. *Proceedings of the National Academy of Sciences USA* **100**, 14,618–14,622 (2003)
- [78] Skalak, R., Keller, S.R., Secomb, T.W.: Mechanics of blood flow. *Journal of Biomechanical Engineering* **103**, 102–115 (1981)
- [79] Skotheim, J.M., Secomb, T.W.: Red blood cells and other nonspherical capsules in shear flow: Oscillatory dynamics and the tank-treading-to-tumbling transition. *Physical Review Letters* **98**, 078,301 (2007)
- [80] Springer, T.A.: Traffic signals on endothelium for lymphocyte recirculation and leukocyte emigration. *Annual Review of Physiology* **57**, 827–872 (1995)

- [81] Succi, S.: *The Lattice Boltzmann equation for fluid dynamics and beyond*. Oxford University Press, Oxford (2001)
- [82] Suresh, S., Spatz, J., Mills, J.P., Micoulet, A., Dao, M., Lim, C.T., Beil, M., Seufferlein, T.: Connections between single-cell biomechanics and human disease states: gastrointestinal cancer and malaria. *Acta Biomaterialia* **1**, 15–30 (2005)
- [83] Suzuki, Y., Tateishi, N., Soutani, M., Maeda, N.: Deformation of erythrocytes in microvessels and glass capillaries: effect of erythrocyte deformability. *Microcirculation* **3**(1), 49–57 (1996)
- [84] Symeonidis, V., Karniadakis, G.: A family of time-staggered schemes for integrating hybrid DPD models for polymers: Algorithms and applications. *Journal of Computational Physics* **218**, 82–101 (2006)
- [85] Tomaiuolo, G., Preziosi, V., Simeone, M., Guido, S., Ciancia, R., Martinelli, V., Rinaldi, C., Rotoli, B.: A methodology to study the deformability of red blood cells flowing in microcapillaries in vitro. *Ann Ist Super Sanita* **43**(2), 186–192 (2007)
- [86] Tran-Son-Tay, R., Sutter, S.P., Rao, P.R.: Determination of RBC membrane viscosity from rheoscopic observations of tank-treading motion. *Biophysical Journal* **46**(1), 65–72 (1984)
- [87] Waugh, R., Evans, E.A.: Thermoelasticity of red blood cell membrane. *Biophysical Journal* **26**(1), 115–131 (1979)
- [88] Weinbaum, S., Tarbell, J.M., Damiano, E.R.: The structure and function of the endothelial glycocalyx layer. *Annual Review of Biomedical Engineering* **9**, 121–167 (2007)